Ain Shams Engineering Journal 14 (2023) 101951

Contents lists available at ScienceDirect

Ain Shams Engineering Journal

journal homepage: www.sciencedirect.com

Thermodynamic optimisation of solar thermal Brayton cycle models and heat exchangers using particle swarm algorithm

O.M. Oyewola [a,c,*], M.O. Petinrin [a], M.J. Labiran [a], T. Bello-Ochende [b]

[a] Department of Mechanical Engineering, University of Ibadan, Ibadan, Nigeria
[b] Department of Mechanical Engineering, University of Cape Town, Cape Town, South Africa
[c] School of Mechanical Engineering, Fiji National University, Suva, Fiji

ARTICLE INFO

Article history:
Received 23 March 2022
Revised 26 May 2022
Accepted 18 August 2022
Available online 10 September 2022

Keywords:
Entropy generation
Irreversibility
Second law analysis
Particle swarm optimization
Brayton cycle

ABSTRACT

In this work, three variants of the Brayton cycle incorporating concentrated solar technologies and dual regenerative systems are modeled. The first variant employs reheat, intercooling, and regeneration, the second applies intercooling and regeneration while the third case involves regeneration only. With the application of the entropy generation method and particle swarm algorithm (PSA), processes with the largest irreversibilities are noted, minimized and the geometric parameters of participating components are optimized.

Results show that irreversibilities occurring in the systems were largely due to finite temperature differences within components. In all cases, the solar receiver and intercooler are the dominant and modest sources of entropy generation respectively. The regenerative system entropy generation is highest in the first case while decreasing in the second and third cases respectively. An improvement in the exergy/availability was observed in the first case, as the first and second law efficiency peaks at 44.9% and 59.68% respectively. Though, with a lower second law efficiency than the former, its percentage network output is equal to the first case at 43%. The aspect ratio, hydraulic diameter, and length of the receiver were observed to vary to enhance greater heat capture and increase the turbine inlet temperature (TIT). The high temperature (HT) regenerator had its geometric properties of a higher magnitude than the low temperature (LT) system as the waste heat recovery is aided by an enhanced heat transfer surface area. In comparison with the single regeneration system, the network output of the dual model was about 33.5% with a significant reduction in the entropy generated, creating a trade-off between operating the system for more power or less generation of irreversibilities.

1. Introduction

The efficiency of the Brayton cycle has been low despite several methods conceived to improve it. Factors such as friction, heat transfer, uncontrolled expansion, and compression amongst others have accounted for vast losses experienced by the cycle. The Brayton cycle has been employed in numerous applications in the power generation and aviation industries due to its low start-up, operation, and maintenance costs [1,2]. The cycle also has other advantages as it can be deployed in modular units, in combination with other power cycles, and work with a variety of fuels [3,4]. Its cycle thermal efficiency is independent of the manner the total heat conductance is distributed between the hot and cold reservoirs [5]. In other to achieve improved efficiency, energy and exergy analysis will be required to identify components and features that facilitate irreversibility generation [6].

Irreversibilities in the heat exchangers have accounted for the bulk of entropy generation and a reduction in net power output [7]. Minimization of the exergy loss will ensure efficient thermal use in the component [8]. Regeneration, reheating and intercooling are some of the processes employed to improve the Brayton cycle's thermal efficiency. Regeneration improves thermal efficiency by

* Corresponding author at: Department of Mechanical Engineering, University of Ibadan, Ibadan, Nigeria.
E-mail addresses: oooyewola001@gmail.com, olanrewaju.oyewola@fnu.ac.fj (O. M. Oyewola).

Peer review under responsibility of Ain Shams University.

Production and hosting by Elsevier

https://doi.org/10.1016/j.asej.2022.101951
2090-4479/

Nomenclature

Symbol

a	Longer side of channel width (m)
A	Area (m^2)
B	Shorter side of channel (m)
BC	Brayton Cycle
c	Specific heat capacity (J/kgK)
D	Dish diameter (m)
d	Channel/dish diameter (m)
Ep	Dish concentrator error (rad)
E	Exergy (J)
$\dot{E}$	Exergy rate (W)
eff	Effectiveness
F	Darcy friction factor
Fig.	Figure
g	Acceleration due to gravity (m/s^2)
h	Convection heat transfer (W/m^2K)
H	Height – Regenerator (m)
HT	High Temperature
I	Irreversibility rate (W)
K	Boltzman's constant
k	Thermal conductivity (W/mK)
l	Length (m)
LT	Low Temperature
$\dot{m}$	Mass flow rate (kg/s)
n	Number of fins/ regenerator channels
NTU	Number of transfer units
Nu	Nusselt Number
P	Pressure (Pa)
Pr	Prandtl number
PSA	Particle Swarm Algorithm
Q	Heat Energy (J)
$\dot{Q}$	Heat energy rate (W)
r	Pressure ratio
Re	Reynolds number
S	Entropy (J/K)
STBC	Solar Thermal Brayton Cycle
t	Thickness of separator plate (m)
T	Temperature (K)
T^*	Apparent sun temperature (K)
TIT	Turbine Inlet Temperature (K)
U	Overall heat transfer coefficient (W/mK)
V	Velocity (m/s)
W	Work (J)

Greek Symbols

η	Efficiency
μ	Dynamic viscosity (kg/ms)
ρ	Density (kg/m^3)
ν	Kinematic viscosity (m^2/s)

Subscripts

1	First/Initial state
2	Second/Final state
atm	Atmospheric
avg	Average
b	Boundary
C	Cold stream
Conc	Concentrator
Conv	Convection
D	Destruction
E	Exit/Outlet
Ext	External
F	Fuel
gen	Generation
h	Hot stream
i	Inlet
int	Internal
loss	Loss due to convection and conduction
Net	Net
o	Outlet
rad	Radiation
rec	Receiver
reg	Recuperator/Regenerator
T	Turbine
Th	Thermal
v	Constant volume

ensuring waste heat recovered from the exhaust gas is used to preheat the working fluid and its use has improved the thermal efficiency of power cycles [9]. Intercooling functions by decreasing the average specific volume of the working fluid, hence, work done by the compressor is also reduced. Reheating is known to increase the turbine work output via an increase in the average specific volume of the gas, thermal energy, and consequently its cycle efficiency [10,11]. This modification to the Brayton cycle has been used exclusively and in combination to improve its performance.

Tyagi [12] studied the effects of intercooling on the performance of an irreversible regenerative Brayton cycle. An optimal value of the intercooling pressure ratio was found to exist at the optimized power output and the corresponding efficiency attains the maximum value. Adibi [13] investigated the effect of the intercooler on the performance and efficiency of the Brayton cycle in ideal and non-ideal conditions. In all the cases studied, the consumed work in the Brayton cycle with an intercooler was less than that obtained without it. Haseli [14] studied three different variants of the Brayton cycle and compared the operational regimes at maximum thermal efficiency, maximum work output, and minimum entropy generation. The study demonstrated that thermodynamic optimization should be based on thermal efficiency or net work output criteria against entropy-based designs. Derivations from literature show that an increase in the net work output from a power cycle can be obtained by intercooling with compression and reheating in the expansion stages at an optimum pressure ratio. However, these modifications increase the exhaust temperature of the process and thus would require recuperation to maximize the resulting cycle efficiency [15].

Isothermal heating can be obtained from renewables aside from fossil fuels providing the basis for the advancement of solarized Brayton cycles over Dish-Stirling technologies [16]. Counterflow recuperators are used in several applications with the reheating process and are effective in increasing the net work output from power cycles that embrace its use [17]. Irreversibilities arising from its use is mostly due to heat transfer through a finite temperature difference and friction with fluid flow[7]. Bejan et al. [18] noted the major processes which foster entropy generation in a solar configuration as; sun-receiver heat interaction, receiver–environment heat transfer, and the irreversibility due to components in the cycle. A solar receiver is the most important element in solar hybridization technology and is used to absorb the radiation from the sun to heat a working fluid in its tubes/ducts [19]. Most receivers have an operating range of 500 – 1200 K depending on the

materials used for the tubing fabrication [20]. Hence, there exists an opportunity to improve the working fluid temperature via this component.

The solar receiver, which is sited at the focus of the dish concentrator, is sized to minimize irreversibility formation due to convective and radiative losses and ensure optimal absorption of heat [16,21]. Several designs of receivers have been studied and their effects on the overall flux distribution within its cavity reviewed. The losses at different inclination angles and wind effects were investigated. The modified receiver cavity designed by Sendhil and Reddy [22] had lower convection losses when compared to other designs. The dish concentrator is the most suitable of the concentrating solar technologies (CST) and is capable of heating the working fluid to between 873 K and 1273 K which is required for the Brayton cycle [20,23].

The deterministic and stochastic algorithms have been extensively used in engineering problem optimization. The resources, time, and hardware technologies needed for computing time often limit the researcher's choice [24]. Chen et al[25] deduced using the NGSA-II algorithm that a linear relationship exists between the net work output from a binary Brayton cycle and efficiencies of the turbomachines. In sizing components for solar thermal applications, the leaf frog algorithm was used to obtain the optimal geometry for components in an STBC variant. [15,17]. Jansen et al. [1] investigated combined open and closed looped STBCs models with either one or two regenerative units, the result gave preference to the single over the double regenerative process. An investigation into the reheating and intercooling effects on three STBC models showed that greater entropy minimization and net power output were obtained for the intercooler variant over other configurations [15]. Stochastic algorithms have the unique characteristics of handling several complex constraints and require limited knowledge of mathematical methods unlike their deterministic counterpart [26,27]. In a study on the use of the stochastic algorithms available, the genetic algorithm was observed to be the preferred option followed by the particle swarm algorithm (PSA) [26]. With the advancement of computational techniques, the PSA has witnessed enhanced adoption in engineering, computing science, automation, robotics, physics, and mathematics field. Its features of enhanced robustness, greater control, and ability to handle complex optimizations make it suitable for a thermodynamic study [28].

Previous works have opined that the addition of a recuperative heat exchanger improves the thermal efficiency of solar Brayton cycles, though with a concomitant increase in the system's irreversibility. Such studies have focused on the thermodynamic design of STBCs with single recuperative units using deterministic optimization techniques. However, from available literature, studies have not been explicitly performed on open-air STBCs with the dual regenerative system. Also, literature is very limited on the use of any of the stochastic algorithms for the optimization of open-air STBCs. Thus, in this work, a dual serial recuperative system is incorporated into the STBC model to improve waste heat recovery. It is anticipated, that the performance of the heat exchangers for the dual system would further reduce irreversibilities generation and improve the net power output. The second law analysis would be used to locate the process and components where the largest irreversibilities occur within the STBC model [6]. The optimization of the STBC model would be performed to exploit the simplicity and robustness of the stochastic optimization tool - the particle swarm algorithm. MATLAB is used as the programming platform to model and perform the optimization while CYCLE Tempo is used for result validation. The results from the analysis are intended to stimulate further ways to improve and enhance the deployment of small-scale STBCs.

2. System description

Plate-type recuperators, dish-mounted modified cavity receivers, and proprietary automotive turbochargers configured as turbomachines were used in the setup for the STBC systems [22,29]. The cases to be investigated are shown in Figs. 1-3 and detailed below;

Case 1: Intercooling combined with low temperature (LT) and high temperature (HT) recuperators plus reheat. The working fluid undergoes multiple compression and intercooling before flow from its HP compressor is routed through a serial LT and HT recuperator to recover waste heat.
Case 2: Intercooling combined with LT and HT recuperators.
Case 3: A Simple Brayton Cycle (BC) with LT and HT recuperators.

2.1. Receiver and reheater model for the solar concentrator

Fig. 4 shows the modified cavity receiver/ reheater unit to be used for increasing the temperature of the working fluid before it undergoes expansion in the turbine. Amongst other receiver types studied, it was shown that its convection losses decrease with an increase in the inclination angle [22]. Also, copper was selected as the material of the receiver tubes for its high thermal conductivity [21].

A rectangular tubing system is used for the analysis and its wall area is expressed as the difference between the surface area of the hemispherical shell and the circle,

$$A_w = A_{hemisphere} - A_{circle} \tag{1}$$

$$A_w = \frac{1}{4}\pi\left(3D^2 - d^2\right) \tag{2}$$

The width of the tube, a, is expressed as.

$$a = \frac{D_{h,rec}}{2}\left(\left(\frac{a}{b}\right)_{rec} + 1\right) \tag{3}$$

The aperture diameter is written in terms of the tube dimension as.

$$d_{rec} = \sqrt{\frac{D_{h,rec}L_{rec}\left(\left(\frac{a}{b}\right)_{rec} + 1\right)}{4\pi}} \tag{4}$$

From [22], for minimum convection losses,$A_w = 8A_a$, substitute for A_w into equation (2);

$$D = \sqrt{3d} \tag{5}$$

Assuming $\dot{Q}_{loss,rad} \simeq \dot{Q}_{loss,conv}$ then the Nusselt number is given as [31].

$$Nu_d = 0.698Gr_d^{0.209}(1+\cos\beta)^{0.968}\left(\frac{T_w}{T_\infty}\right)^{-0.317}\left(\frac{d}{D}\right)^{0.425} \tag{6}$$

Using the heat transfer coefficient relation with the Nusselt number,

$$h_{conv} = \frac{Nu_d k}{D} \tag{7}$$

The radiative and convective heat loss from the receiver cavity is written as [31];

$$\dot{Q}_o = 1.396Gr_d^{0.209}(1+\cos\beta)^{0.968}\left(\frac{T_w}{T_\infty}\right)^{-0.317}\left(\frac{d}{D}\right)^{0.425}\left(\frac{kA_a}{D}\right)(T_w - T_\infty) \tag{8}$$

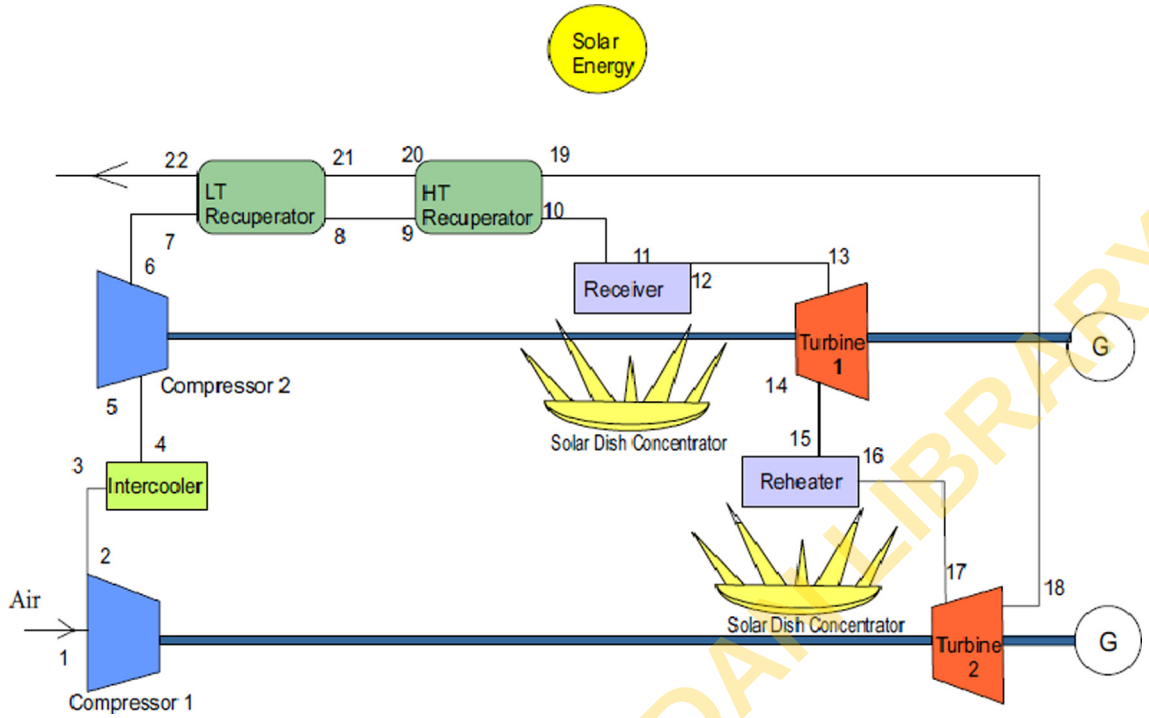

Fig. 1. Case 1: STBC with Intercooling, Reheat, and Regeneration.

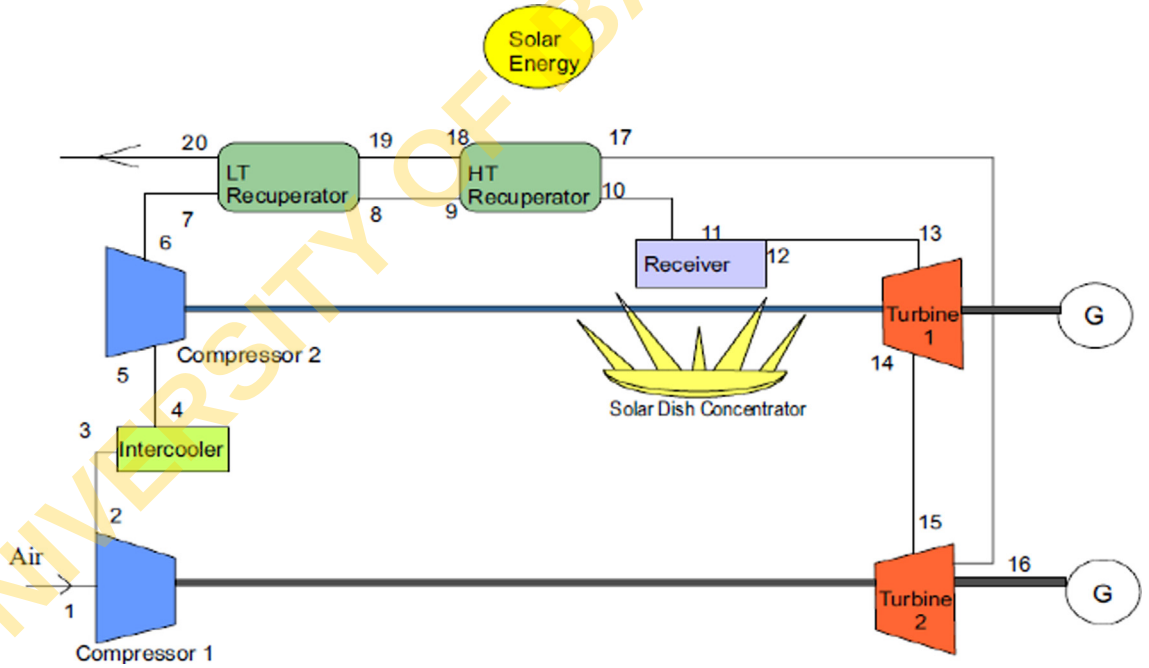

Fig. 2. Case 2: STBC with Intercooling and Regeneration only.

Hence the net heat absorbed is calculated using the receiver sizing algorithm as [32];

$$\dot{Q}_{net,rec} = p_o + p_1 d_{rec}^{0.5} + p_2 d_{rec} + p_3 d_{rec}^{1.5} + p_4 d_{rec}^{2} + p_5 d_{rec}^{2.5} + p_6 d_{rec}^{3} + p_7 d_{rec}^{3.5} + p_8 d_{rec}^{4} + p_9 d_{rec}^{4.5} + p_{10} d_{rec}^{5} \quad (9)$$

The entropy generated in the receiver is then calculated using;

$$\dot{S}_{gen,rec} = -\frac{Q^*}{T^*} + \frac{\dot{Q}_o}{T_o} + \dot{m} c_p ln \frac{T_e}{T_i} - \dot{m} R ln \frac{P_e}{P_i} \quad (10)$$

Q^* is taken as the sum of the net absorbed heat transfer rate and the heat loss rate and T^* is taken as approximately 4500 K [33].

2.2. Recuperator component

The recuperator serves as a means of reducing and increasing the thermal energy of the exhaust gas and incoming charge respectively. The counter flow plate-type design shown in Fig. 5 is used for the present analysis. The mathematical formulations for both the LT and HT recuperator are shown below;

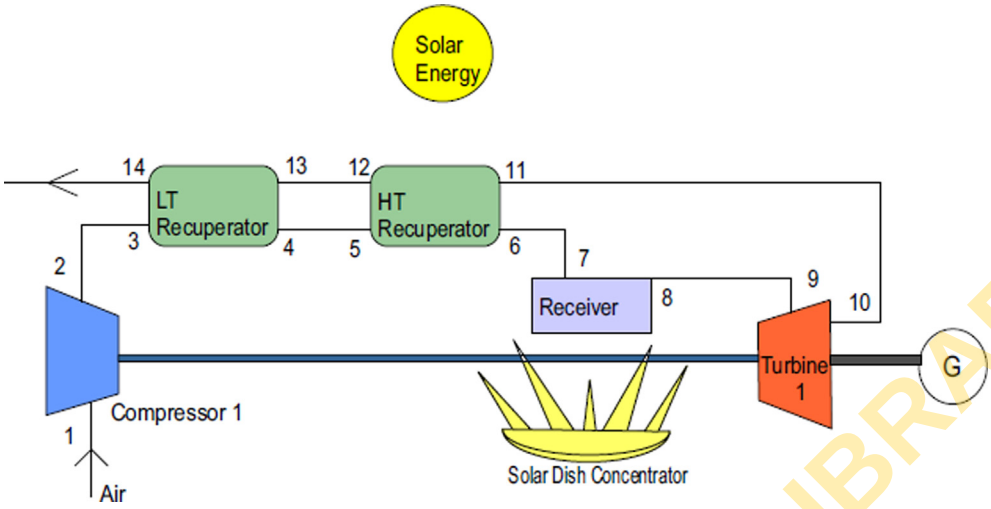

Fig. 3. Case 3: STBC with Regeneration only.

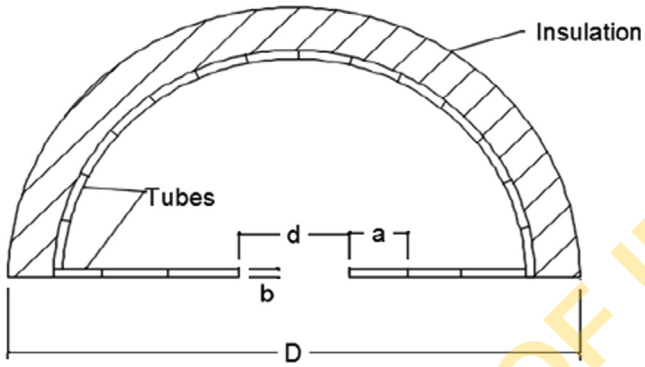

Fig. 4. Schematic of a Modified receiver system [30].

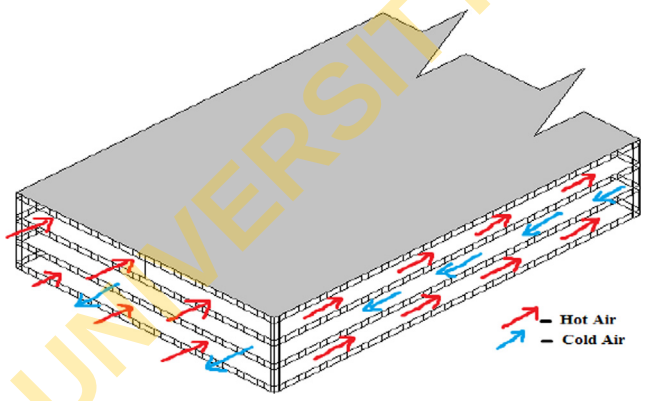

Fig. 5. Cross-section of the counterflow recuperator design.

The number of channels in the overall recuperator height, H is given as.

$$n = \frac{H}{t+b} \tag{11}$$

The channel height, b is.

$$b = D_{h,reg}\frac{\left(\frac{a}{b}\right)_{reg}+1}{2\left(\frac{a}{b}\right)_{reg}} \tag{12}$$

Rearranging the hydraulic diameter, the mass flow rate through a single channel is.

$$\dot{m}_c = \frac{2\dot{m}}{n} \tag{13}$$

The channel surface area is.

$$A_{s,reg} = 2(a+b)L_{reg} \tag{14}$$

$$A_{s,reg} = D_{h,reg}L_{reg}\left(\left(\frac{a}{b}\right)_{reg}+1\right)\left(1+\left(\frac{a}{b}\right)_{reg}^{-1}\right) \tag{15}$$

The velocity of the working fluid through the channels is.

$$V = \frac{\dot{m}}{\rho ab} = \frac{4\dot{m}\left(\frac{a}{b}\right)_{reg}}{\rho D_{h,reg}^2\left(\left(\frac{a}{b}\right)_{reg}+1\right)^2} \tag{16}$$

The Reynolds number is then calculated.

$$Re = \frac{\rho V D_{h,reg}}{\mu} = \frac{4\dot{m}\left(\frac{a}{b}\right)_{reg}}{\mu D_{h,reg}\left(\frac{a}{b}\right)_{reg}^2} \tag{17}$$

The Nusselt number was calculated from the Gnielinski correlation as [34].

$$Nu_d = \frac{\Pr(f/8)(Re-1000)}{1+12.7(f/8)^{0.5}\left(\Pr^{2/3}-1\right)} \tag{18}$$

where the f, which is the Darcy friction factor is given as.

$$f = \sqrt{0.79In(Re-1.64)} \tag{19}$$

Therefore, the heat transfer coefficient was determined from.

$$h = \frac{kNu_d}{D_{h,reg}} \tag{20}$$

The overall heat transfer coefficient, U is calculated while taking into account, fouling on either side;

$$U = \left(h_{cold}^{-1} + 2R_f + \frac{t}{k} + h_{hot}^{-1}\right)^{-1} \tag{21}$$

The effectiveness and NTU analysis is appropriate for counterflow heat exchangers as its theory is founded on effectiveness and capacity ratio and number of heat transfer units [35]. The NTU is obtained from (22) as;

$$NTU = \frac{UA_s}{\dot{m}c_{p,\min}} \tag{22}$$

and the recuperator's effectiveness is defined as.

$$eff_{reg} = \frac{(1-\exp(-NTU(1-C)))}{(1-C\exp(-NTU(1-C)))} \tag{23}$$

Where the heat capacity ratio, C, is defined in the relationship as;

$$C = \frac{c_{p,\min}}{c_{p,\max}} \tag{24}$$

Therefore, the entropy generation in the recuperator is determined from;

$$\dot{S}_{gen,reg} = \dot{m}c_p In\left[\frac{T_{c,e}T_{h,e}}{T_{c,i}T_{h,i}}\left(\frac{P_{c,e}P_{h,e}}{P_{c,i}P_{h,i}}\right)^{\frac{(1-k)}{k}}\right] + \frac{\dot{m}c_p(T_{m,reg}-T_o)}{T_o} \tag{25}$$

where $T_{m,reg}$ is the arithmetic mean of the temperatures in the fluid streams and is defined as;

$$T_{m,reg} = \frac{T_{c,i}+T_{h,i}+T_{c,e}+T_{h,e}}{4} \tag{26}$$

2.3. Intercooler component

A cross-flow design shown in Fig. 6 is employed and oriented to aid the flow of surrounding air by natural convection through its vertical channels.

Heat transfer occurs through forced convection between the hot fluid and the internal plate surfaces and conduction between the hot and cold surfaces (as labeled in Fig. 6).

The mathematical formulation for the intercooler is as follows.

The number of plates, n, needed is given by.

$$n = W/(t+a) \tag{27}$$

The channel length is given as.

$$a = \frac{D_h((a/b)+1)}{2} \tag{28}$$

and the surface area is.

$$A_s = bL = \frac{D_h((a/b)+1)}{2(a/b)}L \tag{29}$$

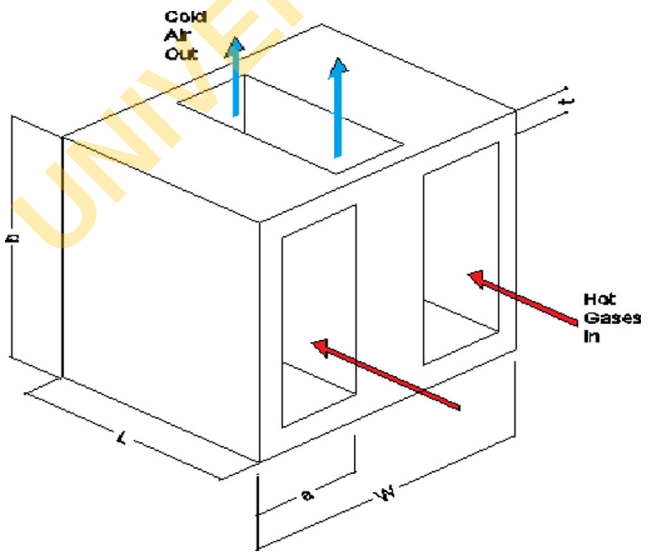

Fig. 6. Schematic representation of the cross-flow intercooler.

The Reynold's number, friction factor, Nusselt number, and heat transfer coefficient were determined respectively from equations (30–33) [34].

$$Re = \frac{4\dot{m}(a/b)}{\mu D_h((a/b)+1)^2} \tag{30}$$

$$f = (0.79In(Re) - 1.64)^{-2} \tag{31}$$

$$Nu_D = \frac{\Pr(f/8)(Re-1000)}{1+12.7(f/8)^{1/2}\left(\Pr^{2/3}-1\right)} \tag{32}$$

$$h = \frac{kNu_D}{D_h} \tag{33}$$

Also, the Rayleigh number, coefficient of volume expansion, Nusselt number, and heat transfer coefficient were estimated respectively from equations (34–37) [15].

$$Ra = \frac{9.81\beta\Pr_{cold}(T_{s,cold}-T_0)a^3}{\nu^2} \tag{34}$$

$$\beta = \left(\frac{T_{s,cold}+T_0}{2}\right)^{-1} \tag{35}$$

$$Nu_D = \left[\left(\frac{576}{Ra(a/b)}\right)^2 + \left(\frac{2.873}{Ra(a/b)}\right)^{0.5}\right]^{-0.5} \tag{36}$$

$$h = \frac{kNu_D}{D_h} \tag{37}$$

The effectiveness of the intercooler can then be calculated after calculating the internal and external heat transfer coefficients.

2.4. Turbomachines

Automotive turbochargers were used to simulate the turbine and compressor parameters. The mass flow rate through the system was taken as that through the compressor of the microturbine. The Garrett range of turbomachines was used in this work because its work range is readily obtainable [29]. A similar study using the same set of turbomachines on an STBC system showed that the maximum efficiency was achieved at a pressure ratio of about 2.5 [15].

The entropy generated in the various turbomachine is evaluated using equation (38) [36].

$$\dot{S}_{gen,turbomachine} = \dot{m}c_p In\frac{T_e}{T_i} - \dot{m}RIn\frac{P_e}{P_i} \tag{38}$$

2.5. Objective function

The Guoy-Stodola theorem expressed in equation (39), is employed to determine the exergy loss from the closed system [37]. It takes to account the ambient temperature and the entropy generated through all the components in the arrangement.

$$\dot{E}_{destroyed} = T_o\sum\dot{S}_{gen} \tag{39}$$

The component entropy generation rate is calculated using equation (40), [36].

$$\dot{S}_{gen} = \dot{m}c_p In\left(\frac{T_{out}}{T_{in}}\right) - \dot{m}RIn\left(\frac{P_{out}}{P_{in}}\right) - \frac{1}{T}\sum Q_{cv} \tag{40}$$

Hence, the net work out of the power cycle is calculated as;

$$\dot{W}_{net} = \dot{Q}_{net} + \dot{m}c_p(T_{in} - T_{out}) - \dot{m}T_o c_p In\left(\frac{T_{in}}{T_{out}}\right) - \dot{E}_{destroyed} \quad (41)$$

Q_{net} is the difference between the net absorbed heat and the heat lost from the system and is obtained using equation (42), [15].

$$Q_{net} = Q^*\left(1 - \frac{T_o}{T_*}\right) \quad (42)$$

Hence the objective function is taken as equation (41) and its parameters are changed to suit the cases investigated.

2.5.1. Pressure and temperature relationship

The temperature and pressures of the working fluid in each process are calculated with the following assumptions.

i. The working fluid is air
ii. There is no change in the mass of the working medium throughout the cycle.
iii. Heat is assumed to be supplied from a constant high-temperature source and not through the combustion of fossil fuels.

All processes commence with the entry of the working fluid into the compressor. This stage has the parameters fixed as 1 atm for P_1 and 300 K for T_1.

The T_{out} and P_{out} were calculated using the compressor pressure ratios. This and other calculations are shown below;

$$P2 = rP1 = rPatm \quad (43)$$

The temperature T_2, after compression, is gotten from $T_1 = T_{atm}$.

$$T2 = T1\left(1 + \left(\left(r_c^{\frac{k-1}{k}} - 1\right)/\eta_{comp}\right)\right) \quad (44)$$

where η_{comp} and k are the turbomachine compressor efficiency and the air's specific heat ratio respectively. The pressure, P_3, and temperature, T_3, of the fluid as it enters the intercooler via duct on node 2–3 is;

$$P_3 = P_2 - (\Delta P_{2-3} * P_2) \quad (45)$$

$$T_3 = T_2 - T_{drop} \quad (46)$$

where $\Delta P_{2\text{-}3}$ and T_{drop}, are the pressure and temperature drop between nodes 2 and 3.

The pressure, P_4, and temperature, T_4, of the fluid after removal of heat generated via compression from the intercooler are shown in equations (47 – 48), [15].

$$P_3 - P_4 = \left[\left(0.79In\left(\frac{4\dot{m}_{ic}(a/b)_{ic}}{\mu D_h(a/b)_{ic}}\right)\right)^{-2}\right]\left[\frac{\left(8\dot{m}_{ic}^2(a/b)_{ic}^2\right)}{\rho((a/b)_{ic}+1)^4}\right]\left[\frac{L}{D_{ic}^5}\right] \quad (47)$$

$$T_4 = T_3 - \left[\left(\frac{A_s h_c}{\dot{m}_c c_{p,h}}\right)(T_{s,c} - T_o)\right] - \left[\frac{\left(A_s \varepsilon_p \sigma_B\left(T_{s,c}^4 - T_o^4\right)\right)}{\dot{m}_c c_{p,h}}\right] \quad (48)$$

The pressure, P_5, and temperature, T_5, of the fluid as it enters compressor *2* via duct on node 4–5 are;

$$P_5 = P_4 - (\Delta P_{4-5} * P_4) \quad (49)$$

where $\Delta P_{4\text{-}5}$ is the pressure drop between nodes 4 and 5.

The pressure, P_6, and temperature, T_6, of the fluid as it exits compressor *2* are given as;

$$P_6 = rP_5 \quad (50)$$

$$T_6 = T_5\left(1 + \left(\left(r_c^{\frac{k-1}{k}} - 1\right)/\eta_{comp}\right)\right) \quad (51)$$

The pressure, P_7, and temperature, T_7, of the fluid as it enters the LT recuperator via duct on node 6–7 is;

$$P7 = P6 - (\Delta P6 - 7 * P6) \quad (52)$$

where $\Delta P_{6\text{-}7}$ is the pressure drop between node 6–7.

Pressure,P_8, out of the LT recuperator is gotten from the mathematical relationship,

$$P_7 - P_8 = \left[\left(0.79In\left(\frac{4\dot{m}_{Ltrec}(a/b)_{Ltrec}}{\mu D_h(a/b)_{Ltrec}}\right)\right)^{-2}\right]\left[\frac{\left(8\dot{m}_{Ltrec}^2(a/b)_{Ltrec}^2\right)}{\rho((a/b)_{Ltrec}+1)^4}\right]\left[\frac{L}{D_{Ltrec}^5}\right] \quad (53)$$

The pressure, P_9, of the fluid as it enters the HT recuperator via duct on node 8–9 is;

$$P_9 = P_8 - (\Delta P_{8-9} * P_8) \quad (54)$$

where $\Delta P_{8\text{-}9}$ is the pressure drop between node 8–9.

The pressure, P_{10}, out of the HT recuperator is obtained from the relationship;

$$P_9 - P_{10} = \left[\left(0.79In\left(\frac{4\dot{m}_{Htrec}(a/b)_{Htrec}}{\mu D_h(a/b)_{Htrec}}\right)\right)^{-2}\right]\left[\frac{\left(8\dot{m}_{Htrec}^2(a/b)_{Htrec}^2\right)}{\rho((a/b)_{Htrec}+1)^4}\right]\left[\frac{L}{D_{Htrec}^5}\right] \quad (55)$$

The pressure, P_{11}, of the fluid as it enters the receiver via duct on node 10–11 is given as;

$$P_{11} = P_{10} - (\Delta P_{10-11} * P_{10}) \quad (56)$$

where $\Delta P_{10\text{-}11}$ is the pressure drop between node 10–11.

The pressure, P_{12}, and the temperature, T_{12}, out of the receiver are as given in equations (57–58) shown as follows;

$$P_{12} = P_{11} - \left[\left(0.79In\left(\frac{4\dot{m}_{rec}(a/b)_{rec}}{\mu D_h(a/b)_{rec}}\right)\right)^{-2}\right]\left[\frac{\left(8\dot{m}_{rec}^2(a/b)_{rec}^2\right)}{\rho((a/b)_{rec}+1)^4}\right]\left[\frac{L}{D_{rec}^5}\right] \quad (57)$$

$$T_{12} = T_{11} + \left(\frac{Q_{net,rec}}{\dot{m}\, c_{p,rec}}\right) \quad (58)$$

The pressure, P_{13}, and temperature, T_{13}, of the fluid as it enters turbine *1* via duct on node 12–13 is;

$$P_{13} = P_{12} - (\Delta P_{12-13} * P_{12}) \quad (59)$$

For maximum power output from the system, the pressure ratio across turbines *1* and *2* must be the same, hence.

$$r_{turb} = \frac{P_{13}}{P_{14}} = \frac{P_{17}}{P_{18}} \quad (60)$$

This ratio, r_{turb} is unknown at first and P_{13}, P_{14}, P_{15}, and P_{16} have to be evaluated.

The pressure, P_{21}, into the LT recuperator, is calculated as follows;

$$P_{21} = P_{22} + \left[\left(0.79In\left(\frac{4\dot{m}_{Ltrec}(a/b)_{Ltrec}}{\mu D_h(a/b)_{Ltrec}}\right)\right)^{-2}\right]\left[\frac{\left(8\dot{m}_{Ltrec}^2(a/b)_{Ltrec}^2\right)}{\rho((a/b)_{Ltrec}+1)^4}\right]\left[\frac{L}{D_{Ltrec}^5}\right] \quad (61)$$

where P_{22} is taken as atmospheric pressure (P_{atm}).

The pressure, P_{20} of the fluid as it exits the HT recuperator, on node 20–21 is calculated as;

$$P_{20} = P_{21} + (\Delta P_{20-21} * P_{21}) \tag{62}$$

where $\Delta P_{20\text{-}21}$ is the pressure drop between node *20–21*.

The pressure, P_{19}, into the HT recuperator, is calculated from.

$$P_{19} = P_{20} + \left[\left(0.79In\left(\frac{4\dot{m}_{Htrec}(a/b)_{Htrec}}{\mu D_h(a/b)_{Htrec}}\right)\right)^{-2}\right]\left[\frac{\left(8\dot{m}^2_{Htrec}(a/b)^2_{Htrec}\right)}{\rho((a/b)_{Htrec}+1)^4}\right]\left[\frac{L}{D^5_{Htrec}}\right] \tag{63}$$

Hence, the pressure, P_{18}, as it exits turbine *1* is calculated as follows;

$$P_{18} = P_{19} + (\Delta P_{18-19} * P_{19}) \tag{64}$$

where $\Delta P_{18\text{-}19}$ is the pressure drop between node 18–19.

Considering the pressure losses on the duct 16–17, pressure$P17$.

$$P17 = P16 - (\Delta P16 - 17 * P16) \tag{65}$$

where $\Delta P_{16\text{-}17}$ is the pressure drop between node 16–17.

The pressure, P_{15}, out of the reheater is gotten from the relationship,

$$P_{15} - P_{16} = \left[\left(0.79In\left(\frac{4\dot{m}_{rec}(a/b)_{rec}}{\mu D_h(a/b)_{rec}}\right)\right)^{-2}\right]\left[\frac{\left(8\dot{m}^2_{rec}(a/b)^2_{rec}\right)}{\rho((a/b)_{rec}+1)^4}\right]\left[\frac{L}{D^5_{rec}}\right] \tag{66}$$

Also, P_{15}, is defined in the relationship between the node 14–15,

$$P15 = P14 - (\Delta P14 - 15 * P14) \tag{67}$$

The pressure, P_{14} exiting Turbine *1* is then obtained using equation (60).

$$P_{14} = \left(\frac{P_{18}P_{13}}{(1-\Delta P_{16-17})(1-\Delta P_{14-15})} + \frac{\Delta P^2_{15-16}}{4(1-\Delta P_{14-15})^2}\right) + \frac{\Delta P_{15-16}}{2(1-\Delta P_{14-15})} \tag{68}$$

The temperature, T_{14}, at the outlet of Turbine *1* is then obtained from equation (72).

$$T_{14} = T_{13}\left[1 - \eta_{turb}\left(1 - \frac{1}{(P_{13}/P_{14})^{\frac{k-1}{k}}}\right)\right] \tag{69}$$

while noting the temperature drop in node 14–15, the temperature, T_{16}, out of the reheater is calculated as;

$$T_{16} = T_{15} + \left(\frac{Q_{net,reh}}{\dot{m}\, c_{p,reh}}\right) \tag{70}$$

Turbine *1* outlet temperature, T_{18}, after accounting for the temperature drop in node *16–17* is obtained from the relationship in equation (71).

$$T_{18} = T_{17}\left[1 - \eta_{turb}\left(1 - \frac{1}{(P_{17}/P_{18})^{\frac{k-1}{k}}}\right)\right] = T_{17}\left[1 - \eta_{turb}\left(1 - \frac{1}{(P_{13}/P_{14})^{\frac{k-1}{k}}}\right)\right] \tag{71}$$

The temperature, T_{10}, and T_{20}, out of the HT recuperator for the cold and hot streams respectively are given as;

$$T_{10} = T_9 + \varepsilon_{HT,recup}(T_{19} - T_9) \tag{72}$$

$$T_{20} = T_{19} - \varepsilon_{HT,recup}\left(\frac{c_{p,c}}{c_{p,h}}\right)(T_{19} - T_9) \tag{73}$$

Hence, the cycle's exit temperature, T_{22} is given by.

$$T_{22} = T_{21} + \varepsilon_{HT,recup}\left(\frac{c_{p,c}}{c_{p,h}}\right)(T_{21} - T_7) \tag{74}$$

Therefore, the cold stream outlet temperature from the LT recuperator is given as.

$$T_8 = T_7 + \varepsilon_{HT,recup}(T_{21} - T_7) \tag{75}$$

A similar formulation would be used for other cases after the removal of appropriate components.

3. Optimisation

The particle swarm algorithm (PSA) is used to solve the objective function of equation (41). The entropy generation term, S_{gen} is minimized to obtain the optimal value for the net work output from the system. The parameters used to perform this optimization are presented in Table 1. A swarm of particles representing the geometric parameters of components is generated and passed through constraints. The objective function is evaluated and the particles with the best results (minimum entropy generation) are termed the personal best. The values are allowed to roam until a global best value is attained with the intended tolerance as stated in the iteration. MATLAB computing software is used to perform this iteration. The turbomachines' geometric parameters are exempted from the optimization process for simplicity of the process.

4. Results and discussion

The system is optimized using definite collector dish radii and design properties got from the Garrett turbomachines. The optimal values are obtained using the particle swarm-based optimizer programmed in MATLAB. The results derived from the cases under investigation are then compared with the reference case to examine the effects of the serial regenerative system. Also, the associated components are analyzed with respect to their optimized geometry, operating conditions, and irreversibilities generated.

Fig. 7a shows the variation of the total heat added, the net work output, and the irreversibility generated internally, for the Case 1 variant. The results from optimization indicate that W_{net} and its associated internal irreversibility approximately reach the same value at a pressure ratio of 2 and mass flow range of 0.808 kg/s. As seen in Fig. 7b, the first and second law efficiencies reach an optimal value of approximately 44% and 59% respectively at this point.

Fig. 8 shows a distribution of the net work output and the irreversibilities generated in the STBC system. A maximum net work output of 43% of the total heat added to the system was derived in Case 1 and 2 while 42% was seen in Case 3. In terms of value, Case 1 can produce more power, however, it is observed that its exergy/availability is the same as in Case 2. The receiver and the regenerators remain the highest contributors to entropy generation within all systems in consideration. The use of multi-

Table 1
PSO Parameters [38].

SN	Parameters	Value
1	Inertia weight (w1)	0.9
2	Inertia weight (w2)	0.9
3	Acceleration factor (c1)	2
4	Acceleration factor (c2)	2
5	Population size (n)	30

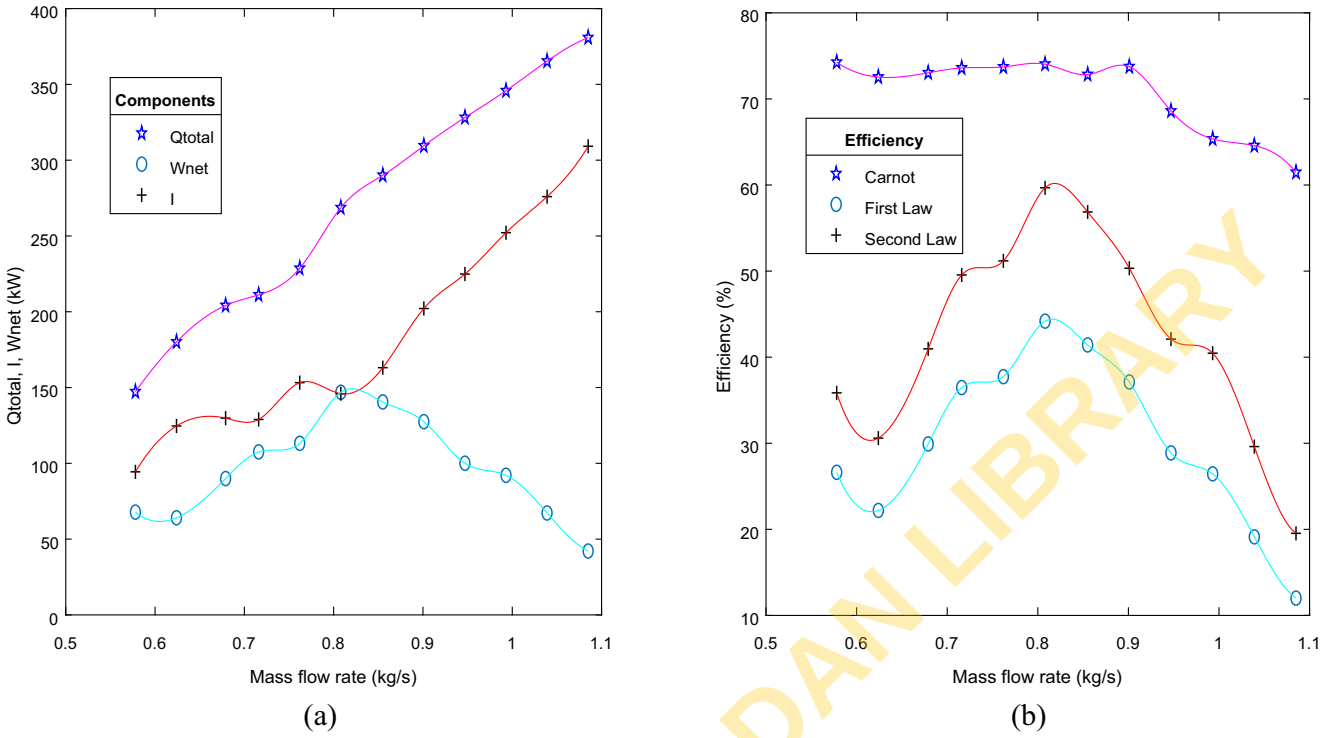

Fig. 7. Plot showing (a) total heat added, the net work output, and the internal irreversibility to the system mass flow rate, (b) comparison of the Carnot, first, and second law efficiency for Case 1.

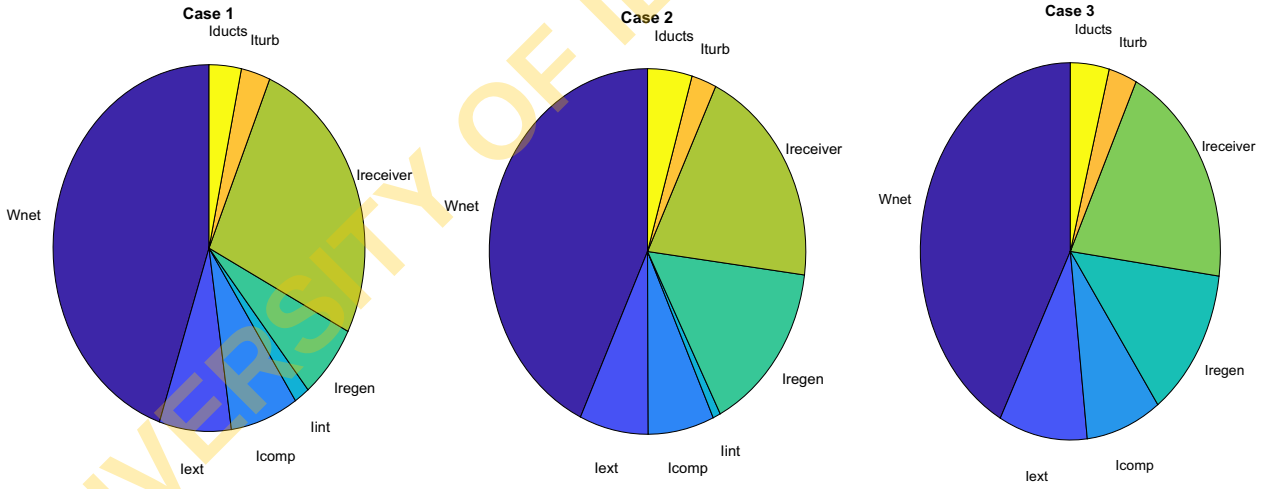

I_{ducts} – Duct irreversibility, I_{comp} – Compressor irreversibility, I_{turb} – Turbine irreversibility, I_{int} – Intercooler irreversibility, $I_{receiver}$ – Receiver irreversibility, $I_{external}$ – External irreversibility, I_{regen} – Regenerator irreversibility, W_{net} – Work out

Fig. 8. Distribution of work and irreversibilities at the optimal work output for Cases 1, 2 and 3.

compression and multi-expansion devices reduced irreversibilities generated via these devices as observed in Cases 1 and 2.

4.1. System components operating conditions and parameter

4.1.1. Regenerator

The impact of the internal irreversibility is observed to be significantly higher than its external irreversibility at any pressure ratio. With the components within the cycle accounting for the internal irreversibility produced [1], the regenerator was observed to be the second most dominant form of irreversibilities formation for Cases 1 and 3 with its values larger at lower mass flow rates as seen in Figs. 9–11. On the contrary, it is seen to be minimal in case 2, this is attributable to the use of multi-expansion systems. Figs. 13–17 show a fair correlation in the optimized parameters aspect ratio and length to the mass flow rate for case 2 dual regenerative system unlike cases 1 and 2. Likewise, the aspect ratio, and length quantities show an increase at higher mass flow rates for cases 1 and 3 as a substantial increase to its surface area is needed for optimal heat transfer. In all cases, the hydraulic diameter is observed to decrease with an increase in working fluid pressure due to an increase in the HT regenerator heat transfer effective-

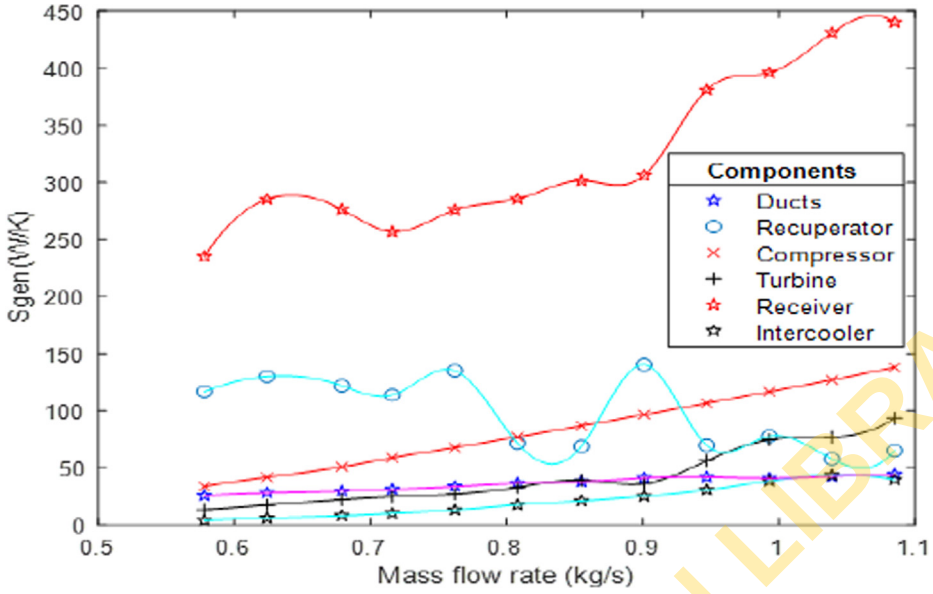

Fig. 9. Distribution in the entropy generated with reference to the mass flow rate (Case 1).

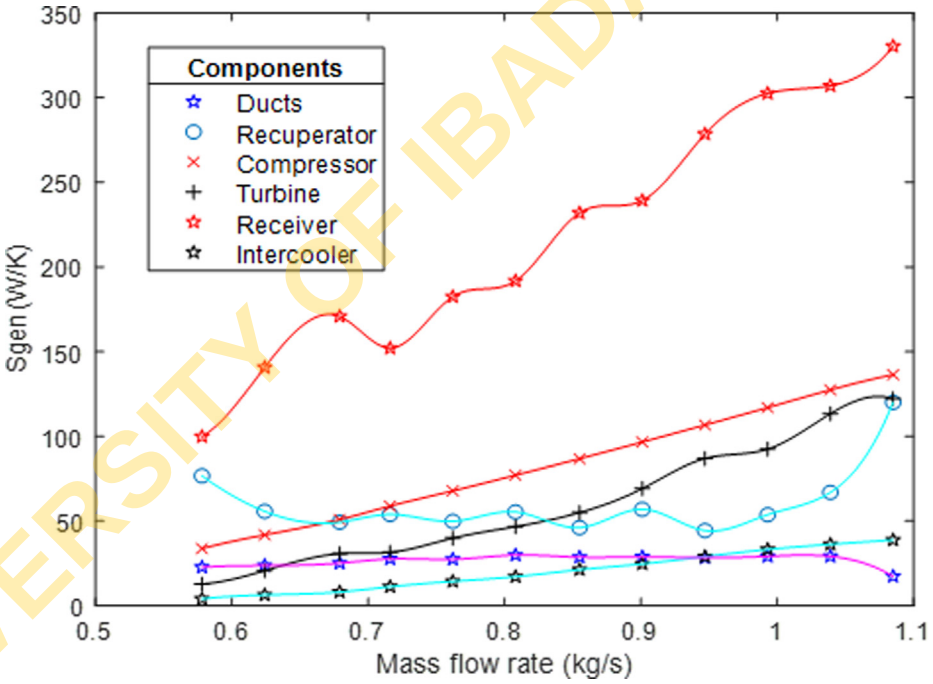

Fig. 10. Distribution in the entropy generated with reference to the mass flow rate (Case 2).

ness. The optimized geometric parameters for the regenerators are higher for the HT than its LT counterpart.

The aspect ratio of the HT recuperator in all cases is higher than its corresponding LT recuperator and increases with the system mass flow as shown in Figs. 12-14. Figs. 15-17 shows that the length of the former is longer than the latter for most of the mass flow ranges. It has the highest value for Case 3 and this is expected as sufficient time is needed for heat transfer between the hot and cold stream since there is a single compression and expansion stage. In all cases, the hydraulic diameter of the recuperator tubes somewhat decreases with the system's mass flow rate.

4.1.2. Intercooler

The intercooler hydraulic diameter is observed to be in the order of lower magnitude compared to the regenerator as seen in Fig. 18. This could be attributed to the slight variation between the ambient temperature and the outlet temperature of the working fluid at the intercooler and its low friction loss which accounts for the low exergy loss from the component.

The figure shows the plot of the channel hydraulic diameter increasing, peaking, and decreasing severally across the system mass flow rate. It is evident from Figs. 19 and 20, that the minimal entropy generation at the post-plateau range was achieved at the lower limit of the constraint for the Case 1 variant.

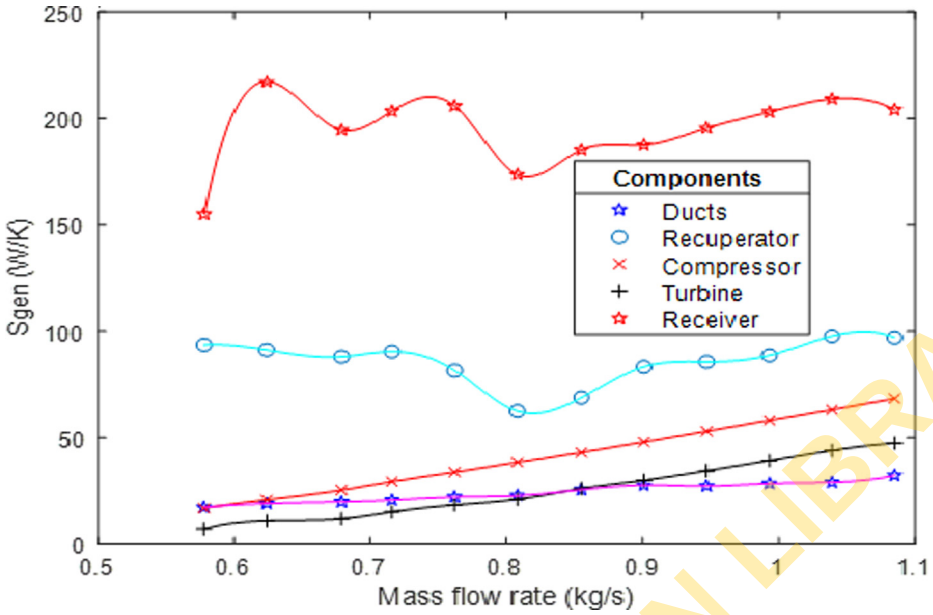

Fig. 11. Distribution in the entropy generated with reference to the mass flow rate (Case 3).

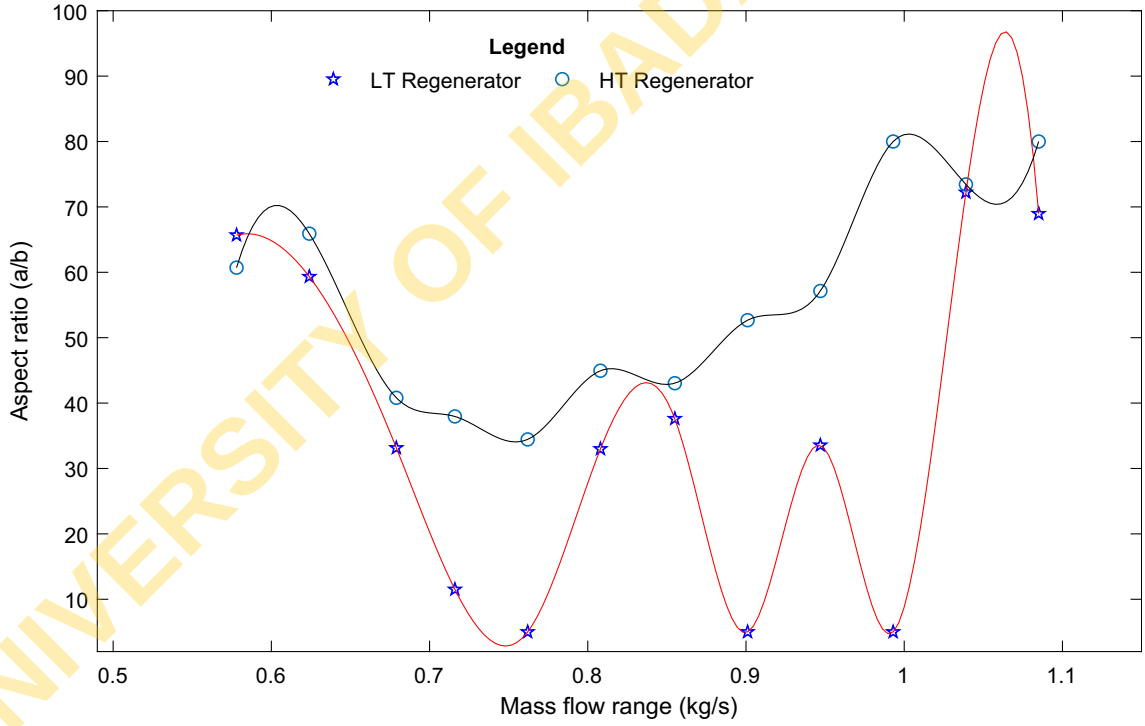

Fig. 12. Case 1 - Relationship of the regenerator aspect ratio to the mass flow rate.

The intercooler length for Cases 1 and 2 rises and peaks at the upper limit as shown in Fig. 19. The length and aspect ratio for both cases is observed to be slightly above the lower limit of the PSA for a mass flow rate of above 0.8 kg/s. This could be due to an increase in the mass flow rate of the hot and cold streams as a result of an increase in the number of channels.

4.1.3. Receiver and reheater

The receiver remains the leading cause of irreversibility for all systems under consideration. The rectangular cross-section absorber tubes were used for this analysis. At lower mass flow rates, there is an increased entropy generation in the receiver due to the receiver aperture increasing to permit more interception of heat. This is a result of the low temperature at the regenerator outlet and the need to increase the turbine inlet temperature (TIT). As the compression ratio increases, the receiver aperture diameter decreases just to allow for sufficient heating of the absorber tubes as the temperature out of the regenerator output is significantly higher than at a low compression ratio. Consequently, as seen in Figs. 21-22, the receiver's hydraulic diameter is observed to

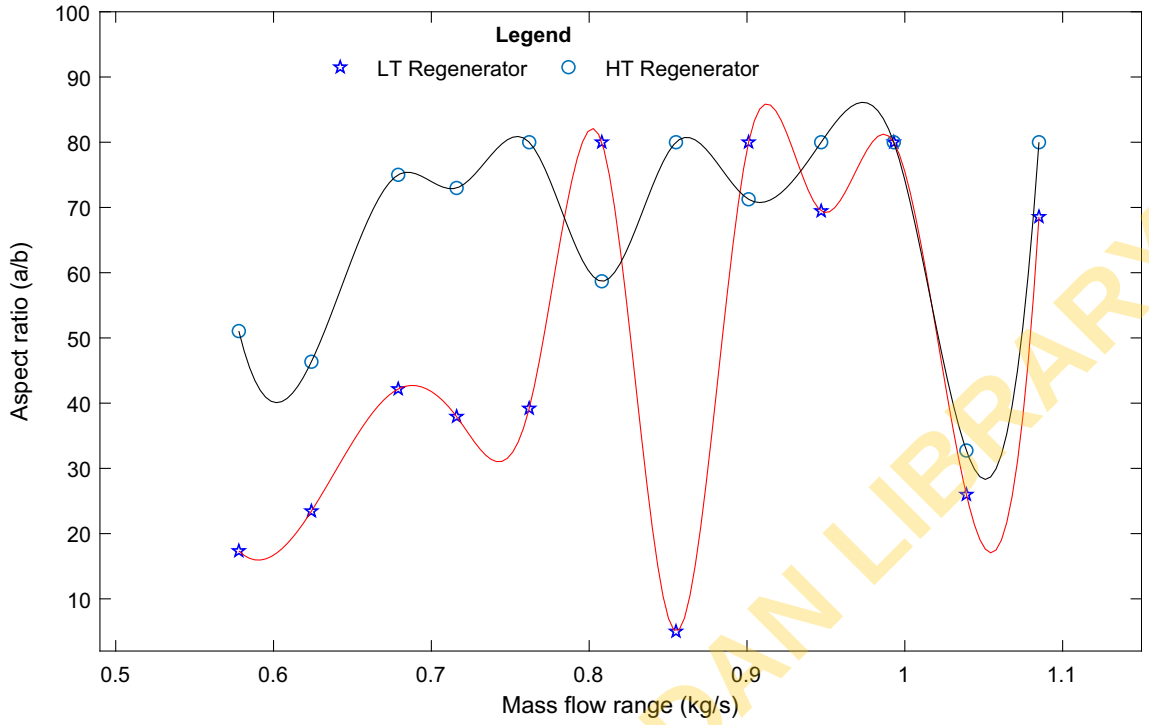

Fig. 13. Case 2 - Relationship of the regenerator aspect ratio to the mass flow rate.

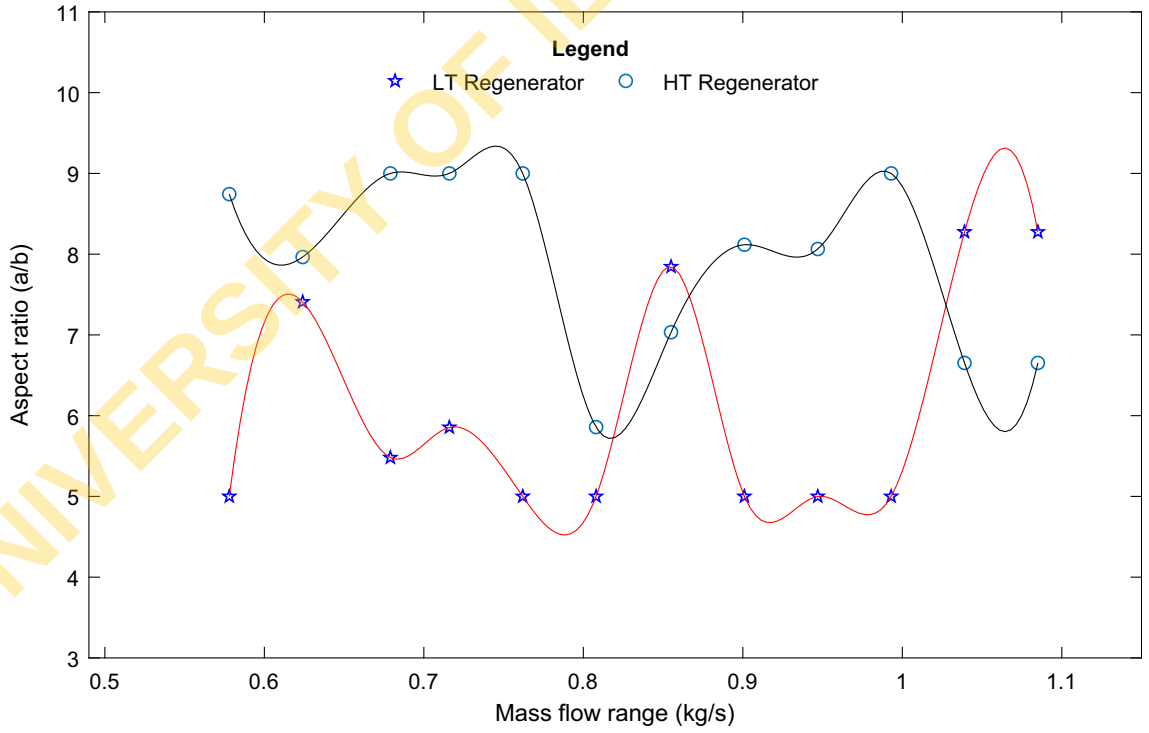

Fig. 14. Case 3 - Relationship of the regenerator aspect ratio to the mass flow rate.

decrease as the system mass flow rate increases and after the plateau, it is then seen to increase. Conversely, Fig. 23 shows the receiver length increasing with the system mass flow rate to ensure sufficient heat interception.

There is an approximately linear relationship between the reheater length, its aspect ratio, and the mass flow rate increases as depicted in Figs. 24 and 25, respectively. This could be attributed to the component aperture increasing to encourage greater heat capture. Several peaks are seen in the figure and are attributed to the maximum absorber surface temperature which is constrained below 1200 K.

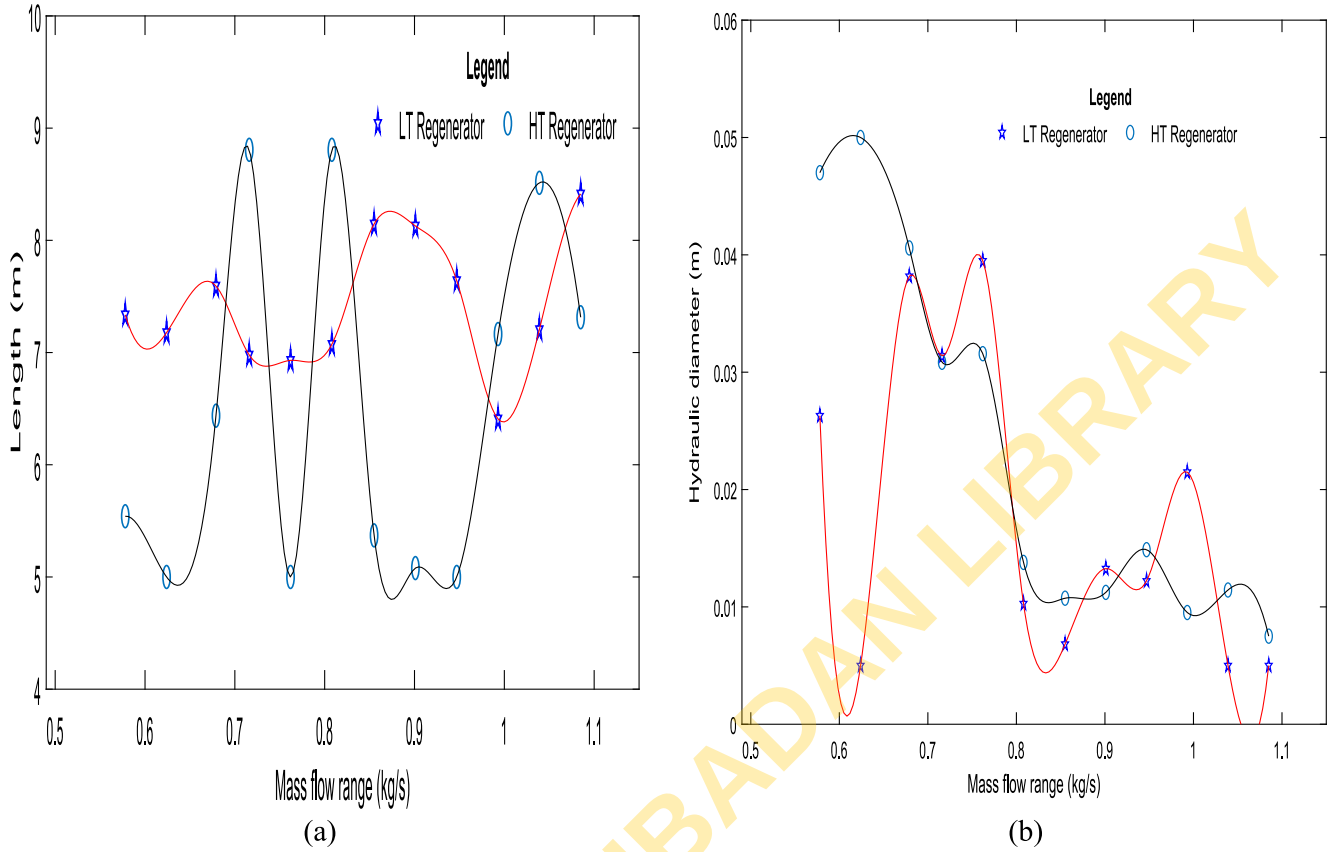

Fig. 15. Plot showing the relationship of case 1 regenerator (a) length to the mass flow rate. (b). hydraulic diameter to the mass flow rate.

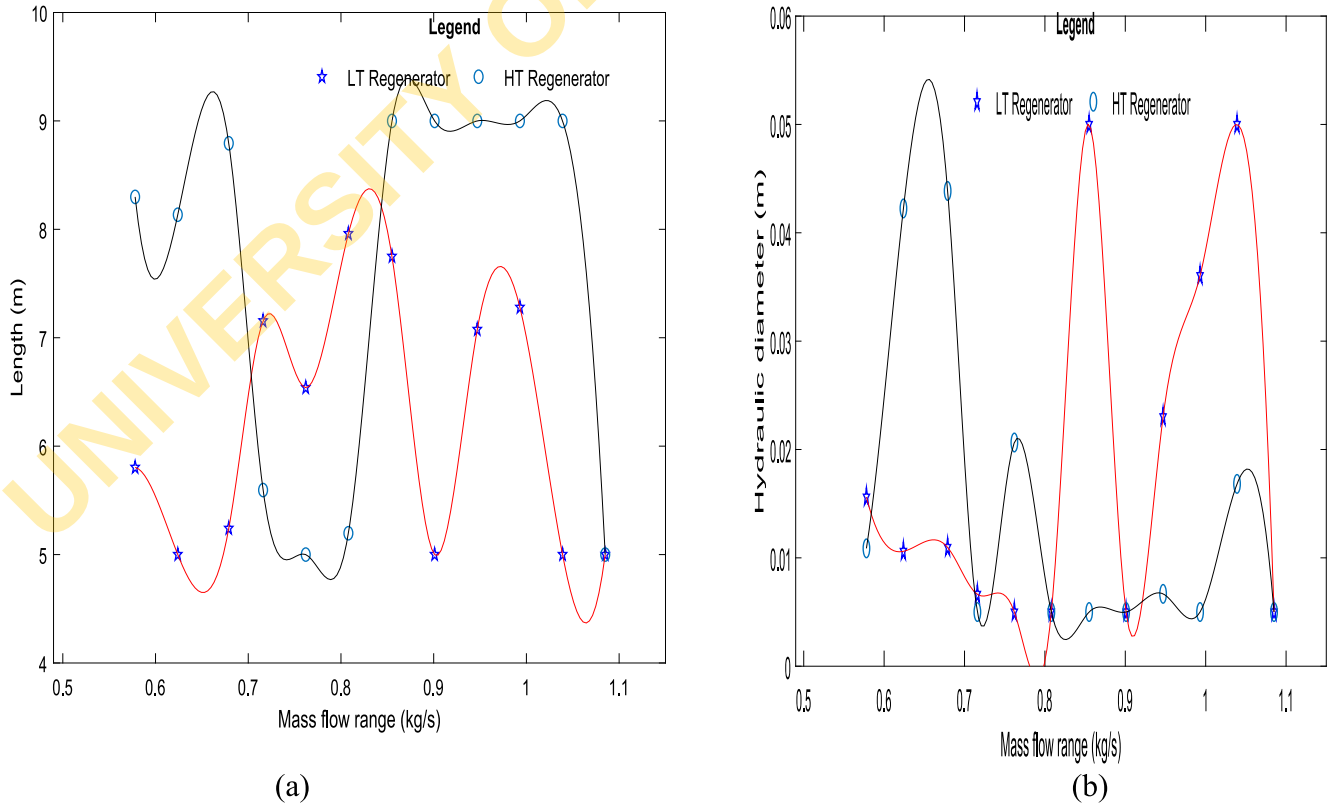

Fig. 16. Plot showing the relationship of case 2 recuperator (a) length to the mass flow rate. (b). hydraulic diameter to the mass flow rate.

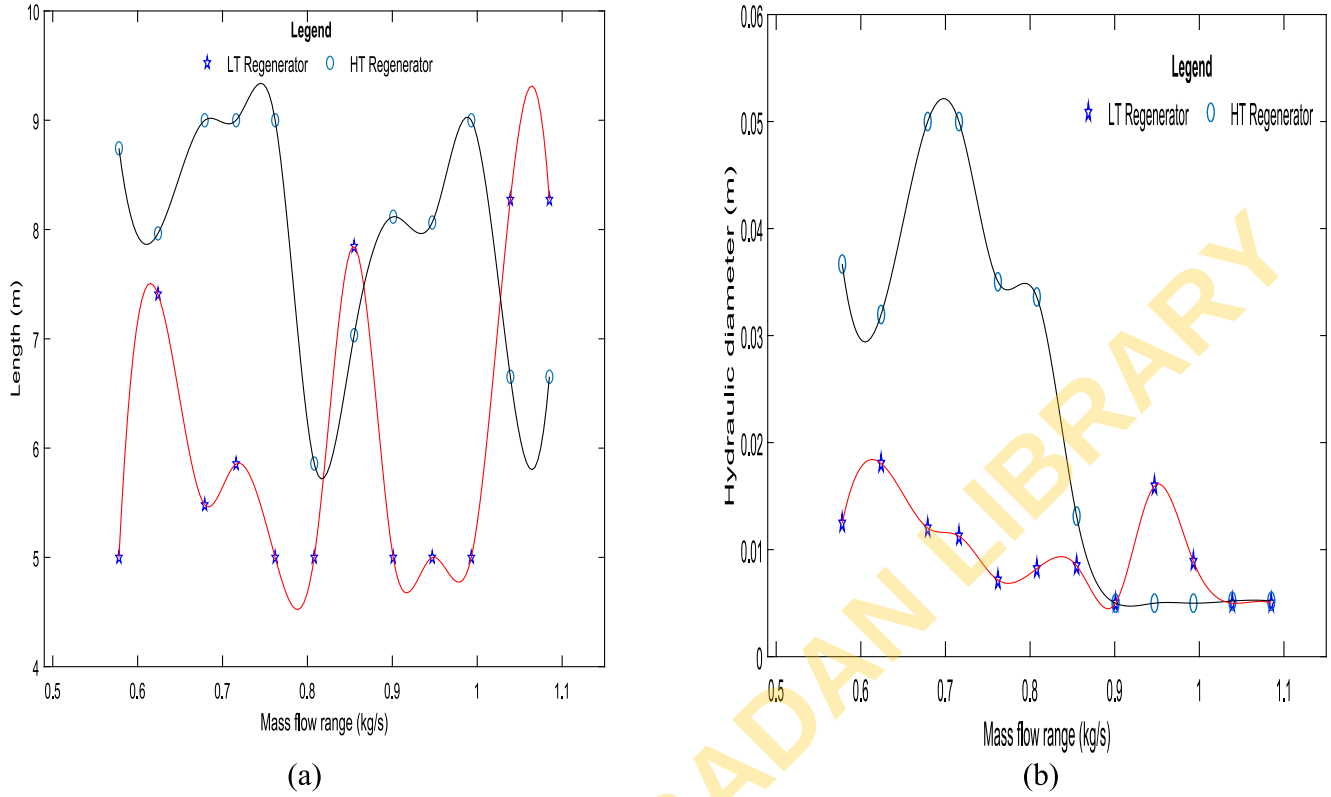

Fig. 17. Plot showing the relationship of case 3 recuperator (a) length to the mass flow rate. (b). hydraulic diameter to the mass flow rate.

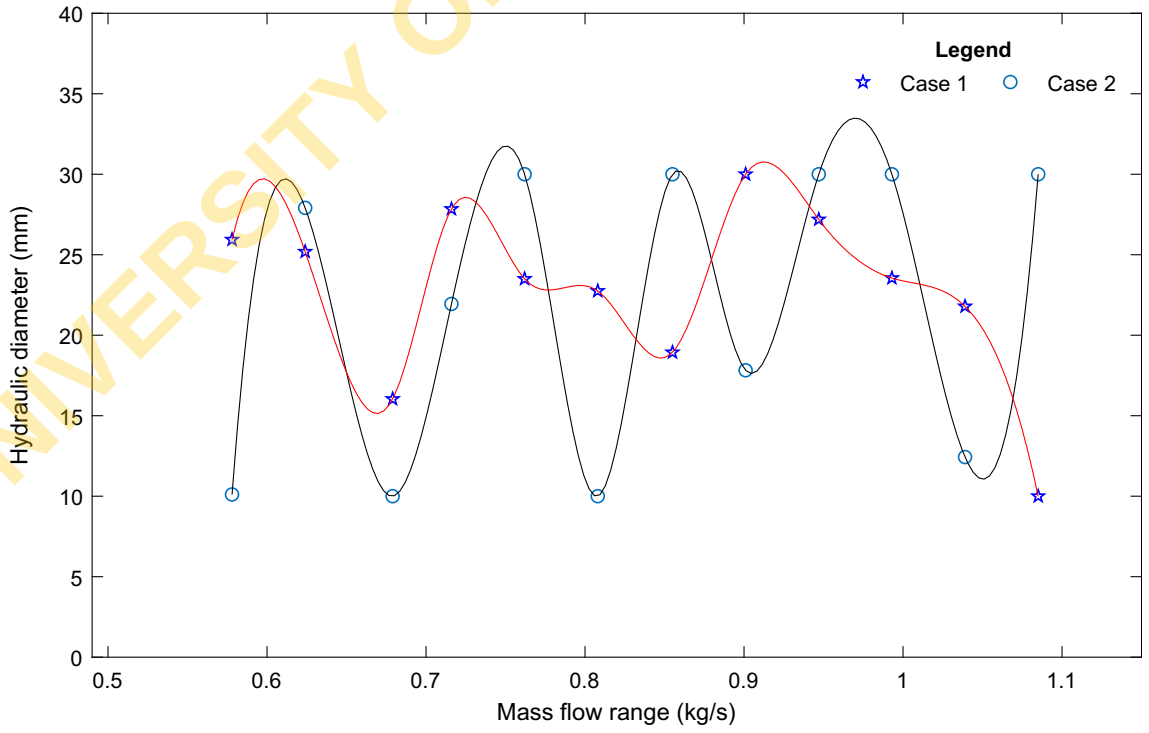

Fig. 18. Plot showing the comparison of the Intercoolers' hydraulic diameter to the mass flow rate.

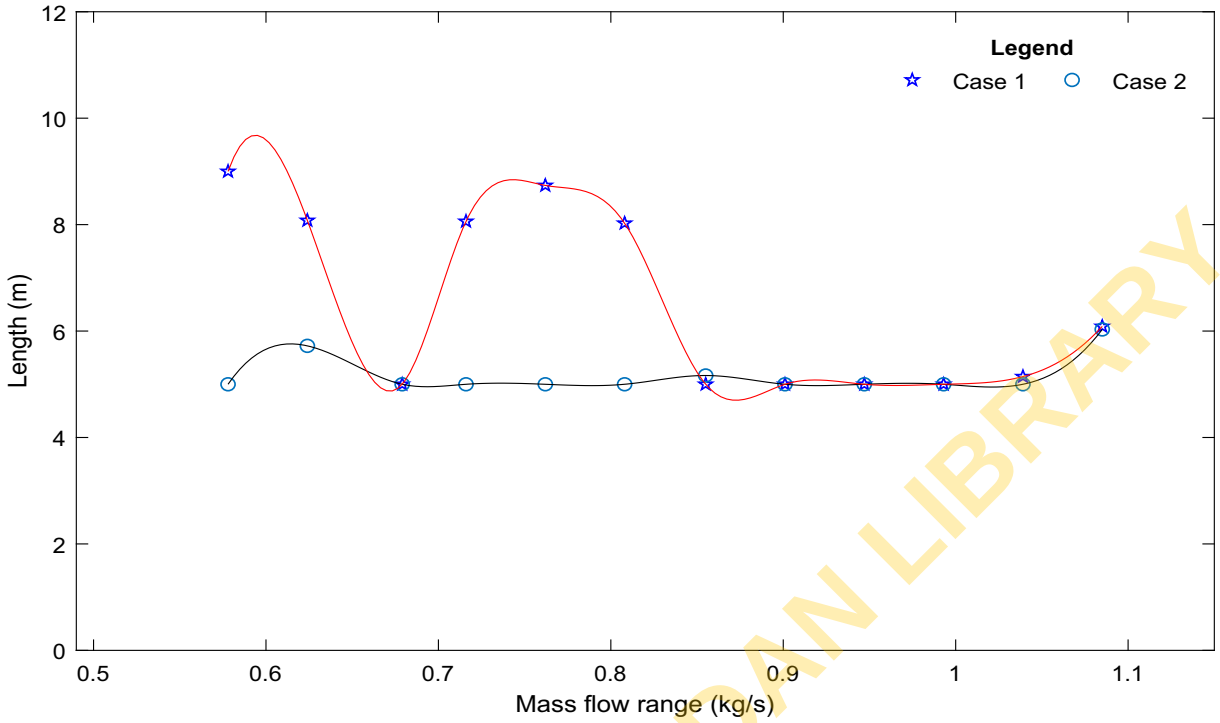

Fig. 19. Plot showing the hydraulic diameter of the intercooler to the mass flow rate.

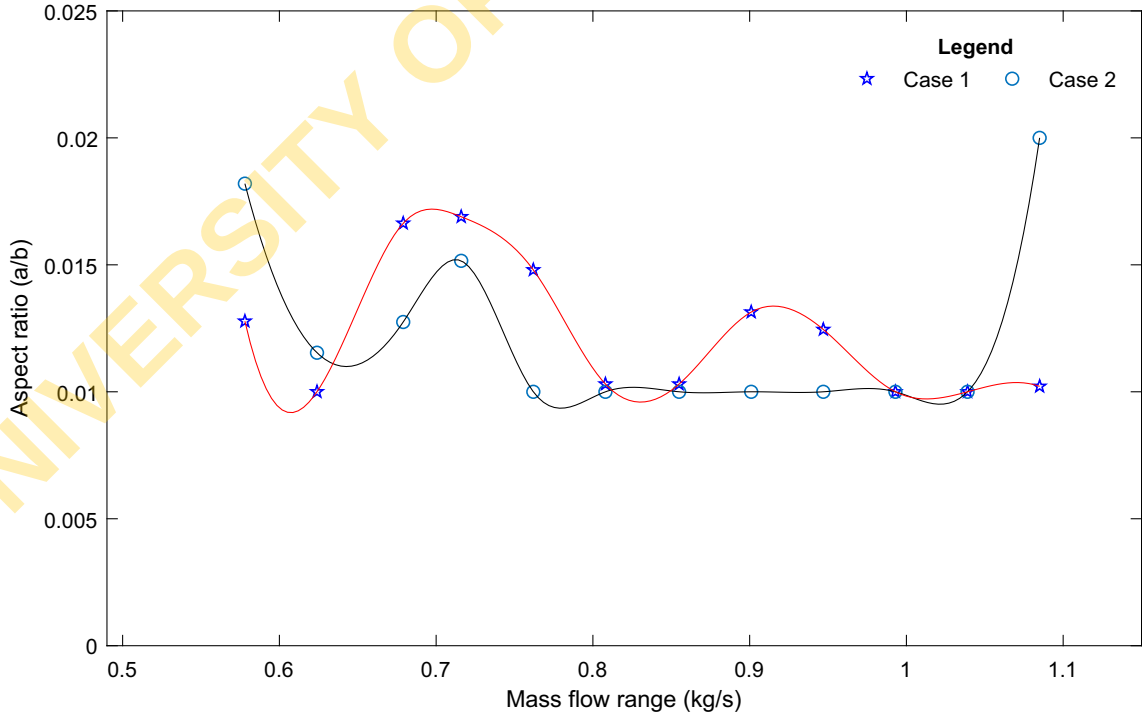

Fig. 20. Plot showing the aspect ratio of the intercooler to the mass flow rate.

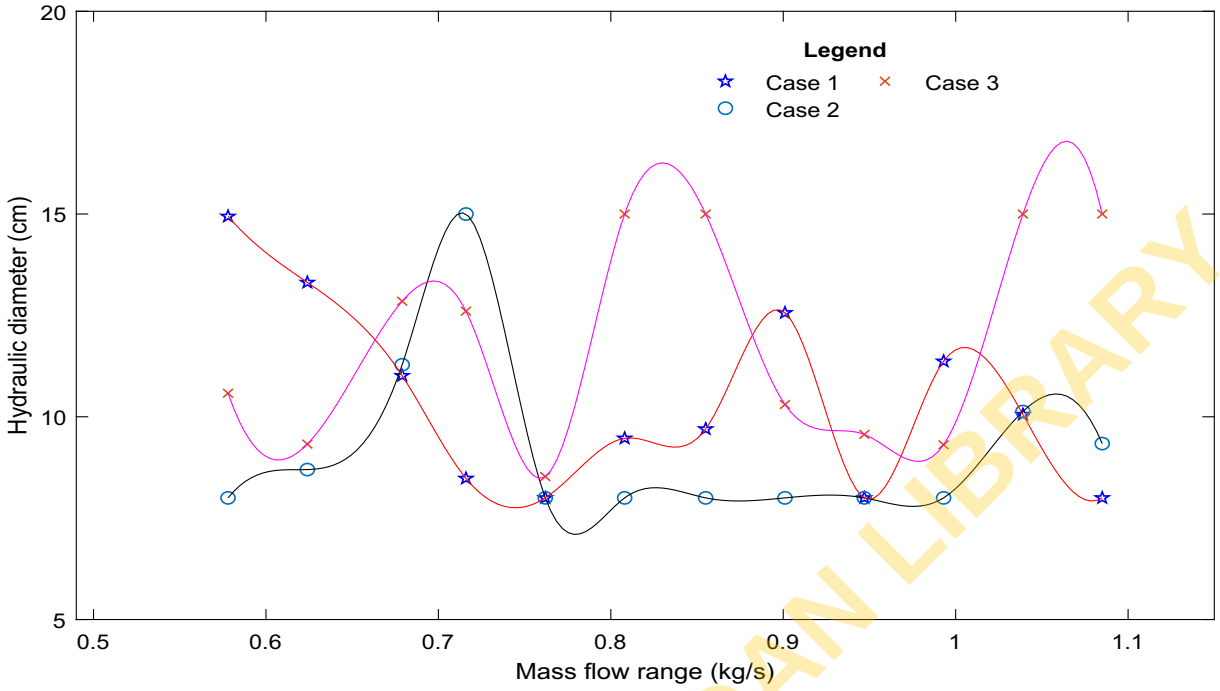

Fig. 21. Plot showing the interaction of the receiver hydraulic diameter to the mass flow rate.

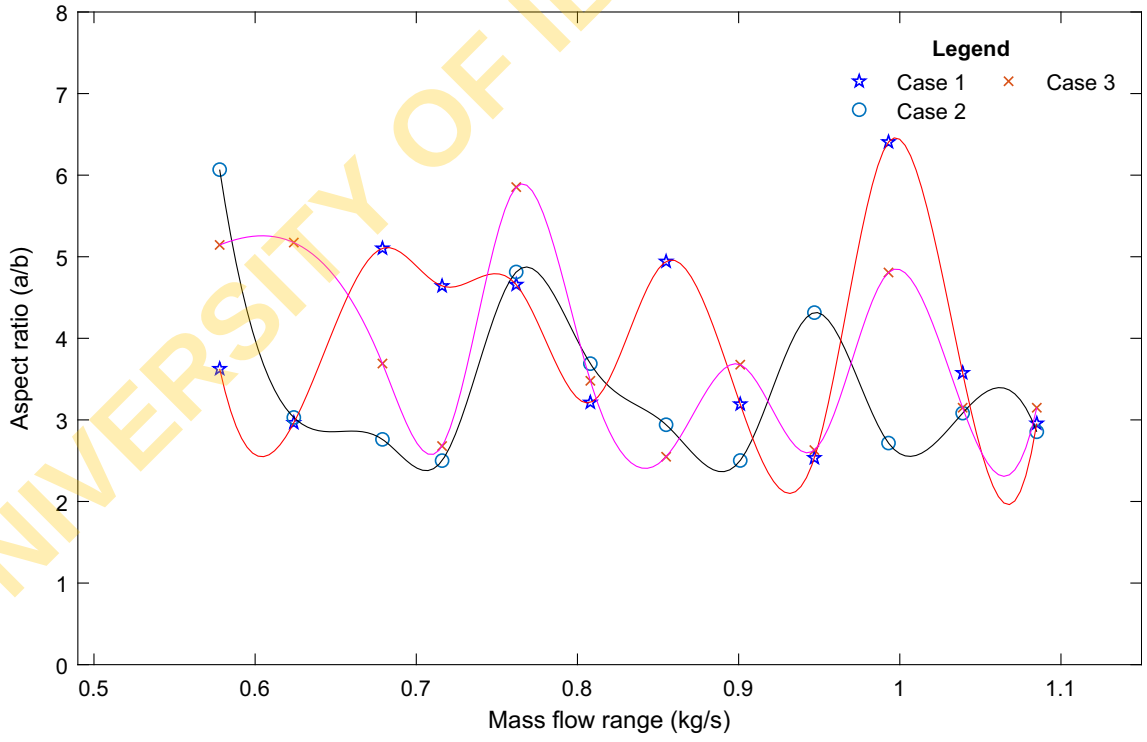

Fig. 22. Plot showing the interaction of the receiver aspect ratio to the mass flow rate.

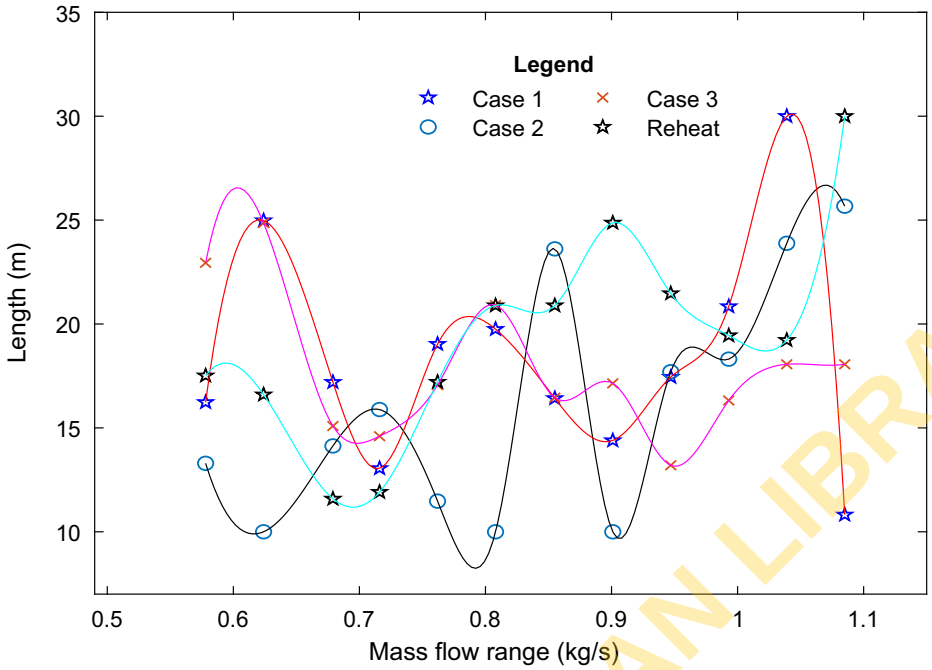

Fig. 23. Plot showing the interaction of the length of the receiver and reheat to the mass flow rate.

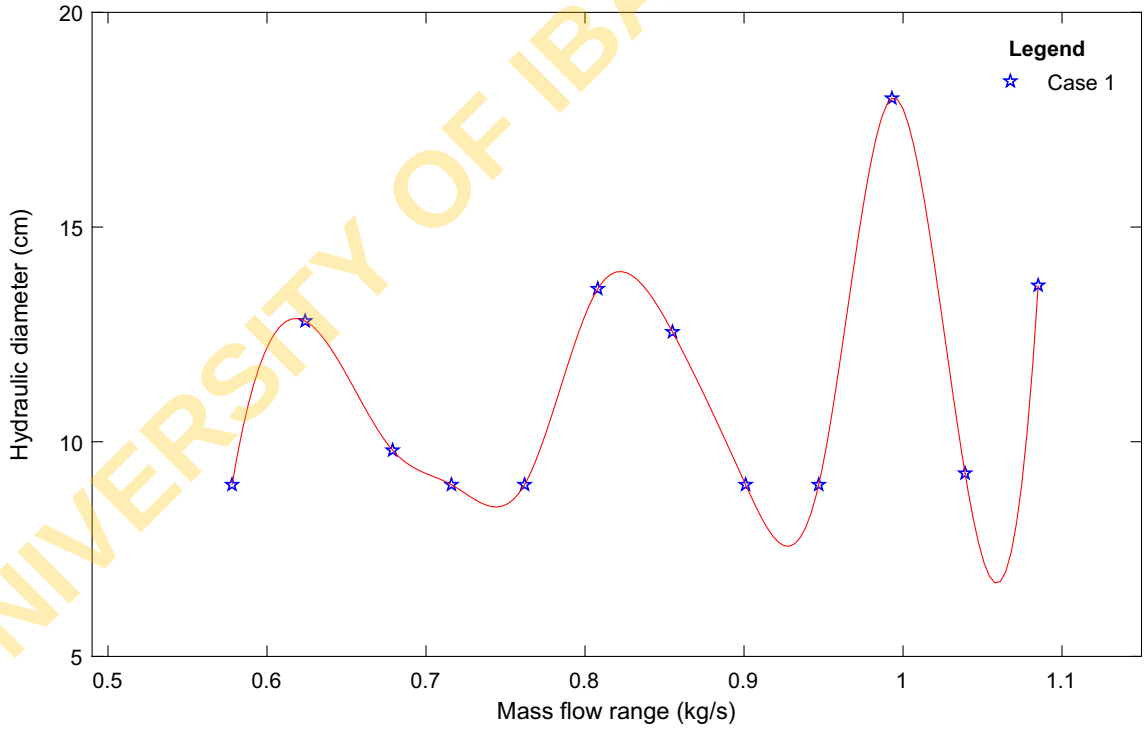

Fig. 24. Plot showing the interaction of the reheater hydraulic diameter to the mass flow rate.

4.2. Comparison of the single and dual recuperative models

As seen in Fig. 26 for Case 1 model, the net work output produced by the model with a dual recuperative system was approximately 33.5% higher than with a single recuperator for the same range of flow rate. The ratio of the irreversibility generated (internal to external) was higher for the latter at low mass flow rates and higher for the former at higher mass flow rates.

The increase in the internal irreversibility generation at higher mass flow rates was largely due to the increased pressure ratio, friction, and other inefficiencies of the participating components. Though, this loss is justified by the corresponding increase in the net power output from the dual regeneration model. In addition, it is observed that operating the dual regenerative system at mass flow rates higher than 0.8 kg/s is overly advantageous as there is an improvement in the net work output over the single regenerator

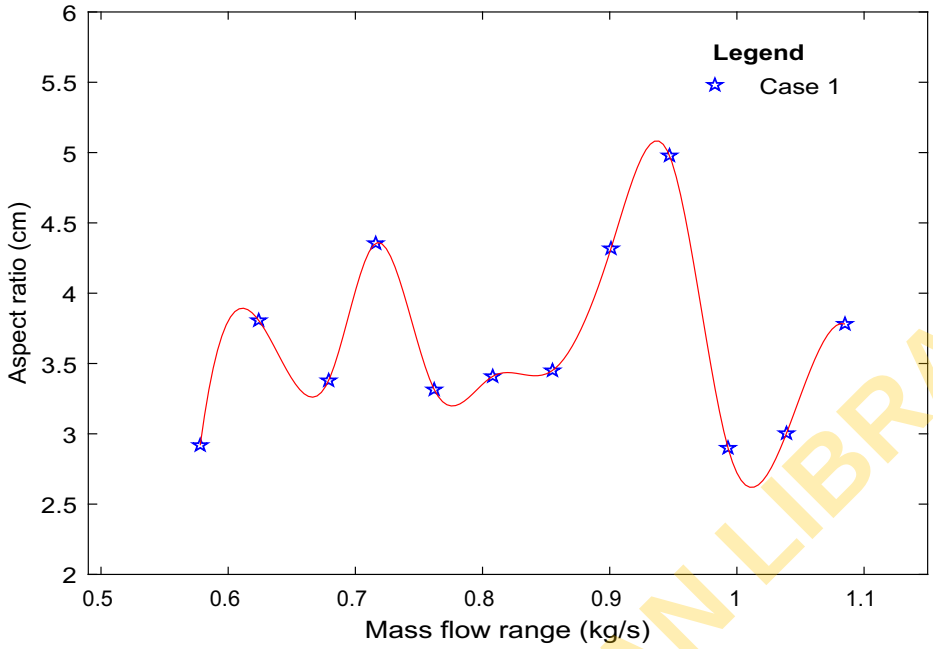

Fig. 25. Plot showing the interaction of the reheater aspect ratio to the mass flow rate.

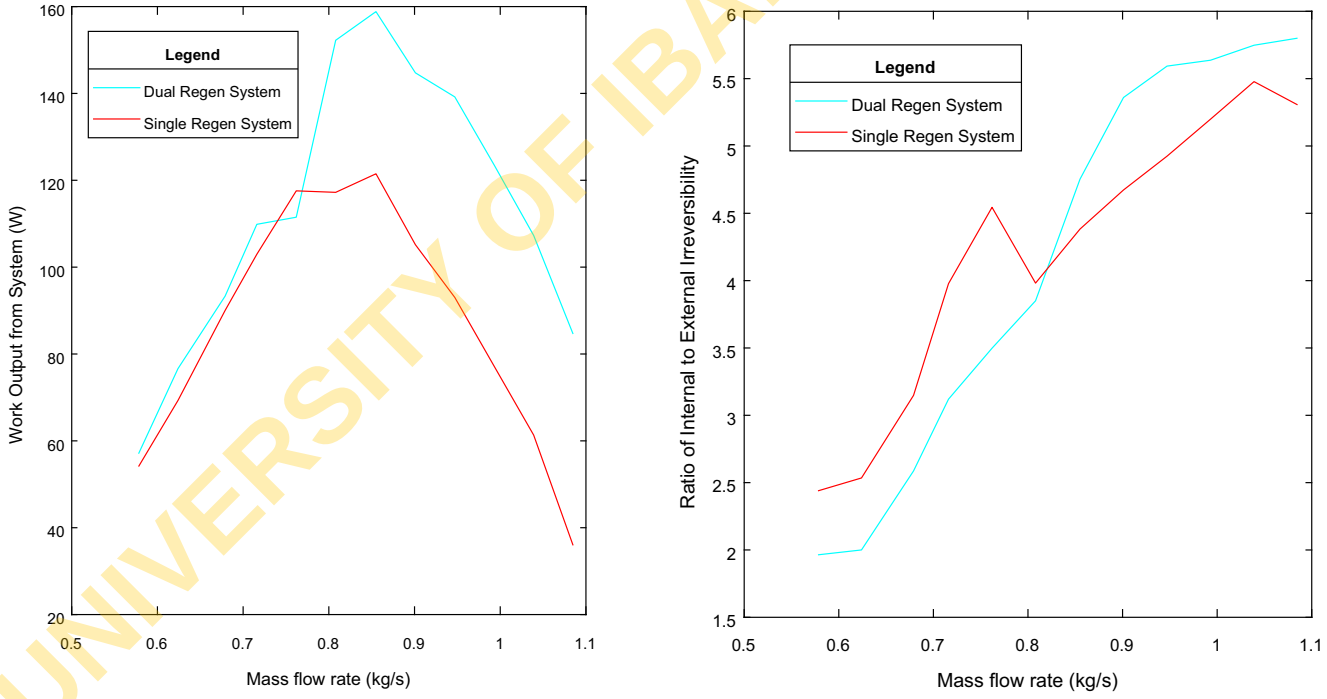

Fig. 26. Plot showing the net work output and the ratio of internal and external irreversibility for the dual and single regenerative systems.

equivalent. However, the system reduces significantly the entropy generated at low pressure ratios with a slightly higher net work output. This leads to a trade-off between STBC operation for higher net work output or lower rreversibility generation.

5. Validation of the STBC model

Proprietary components embedded in the Cycle-Tempo software were used to reproduce the Case 3 variant of the STBC as seen in Fig. 27. The mass flow through all the components was assumed to be constant. As presented in Table 2, the computed results from MATLAB and Cycle-Tempo compared well and were in good correlation. The comparison of the results shows a maximum deviation below 9% for the temperature and pressure parameters which occurs at the exit from the Turbine. The observed variation with a maximum of 9% could be a result of different choices of correlations used in both software for thermodynamic analyses of each of the components.

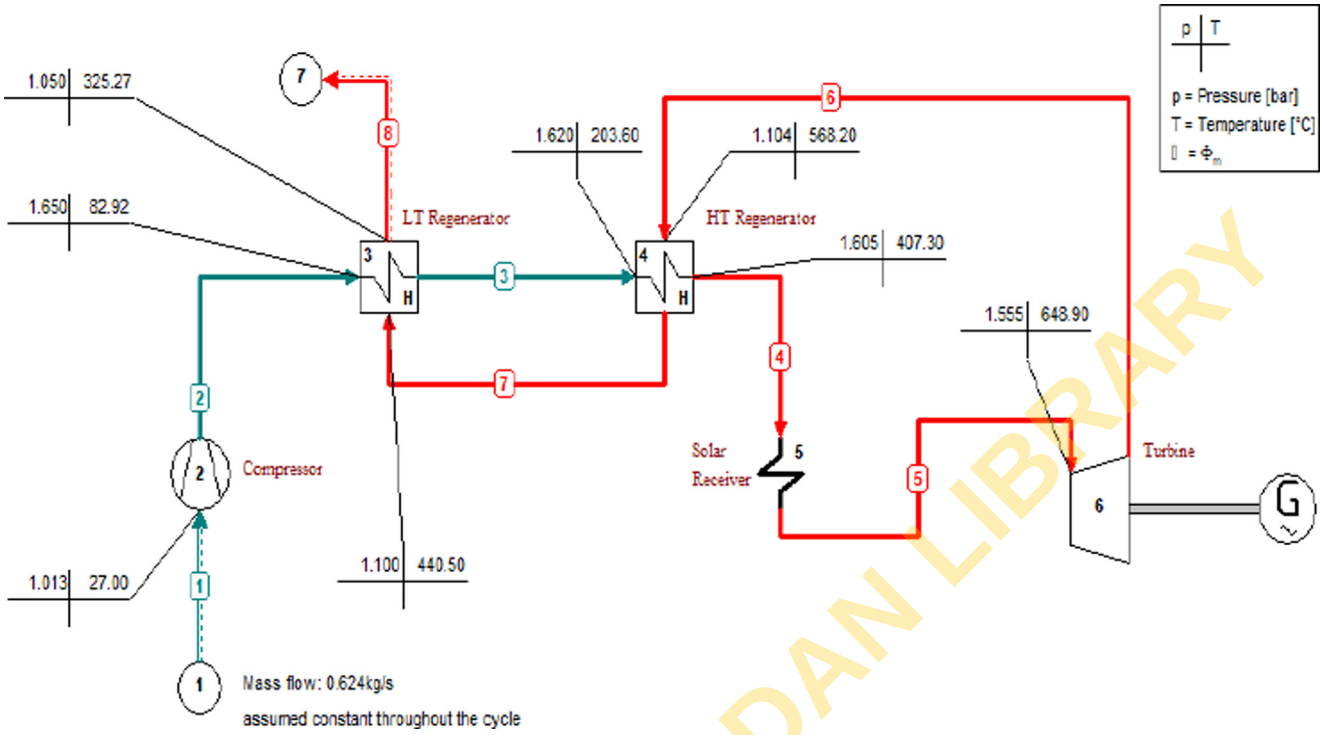

Fig. 27. Simulated Results for STBC Model 3 using Cycle Tempo.

Table 2
Variation of Nodal Temperatures and Pressures obtained for Model 3 from MATLAB and Cycle Tempo.

Node	Temperature (°C)			Pressure (bar)		
	MATLAB	Cycle Tempo	Variation	MATLAB	Cycle Tempo	Variation
1	27.00	27.00	0.0%	1.013	1.013	0.00%
2	81.58	82.92	−1.6%	1.621	1.650	−1.79%
3	79.58	82.92	−4.2%	1.614	1.650	−2.23%
4	206.46	203.60	1.4%	1.614	1.620	−0.37%
5	204.76	203.60	0.6%	1.608	1.620	−0.75%
6	419.38	408.00	2.7%	1.607	1.605	0.12%
7	417.73	408.00	2.3%	1.607	1.605	0.12%
8	661.97	648.90	2.0%	1.588	1.555	2.08%
9	659.97	648.90	1.7%	1.581	1.555	1.64%
10	573.52	568.20	0.9%	1.022	1.104	−8.02%
11	571.52	568.20	0.6%	1.018	1.104	−8.45%
12	428.98	440.50	−2.7%	1.017	1.100	−8.16%
13	426.98	440.50	−3.2%	1.013	1.100	−8.59%
14	303.07	325.27	−7.3%	1.013	1.050	−3.65%

6. Conclusion

This study focuses on the implementation of exergy analysis and its utilization in the design and operation of components of three solar thermal Brayton cycle models. The optimization is carried out on a system basis against individual optimizations of system components using the particle swarm algorithm (PSA). The test cases were modeled by incorporating the dish concentrator system and a dual recuperative system. The first case employed intercooling and reheating means; the second case included intercooling only while the third is devoid of the intercooler and reheater.

Net work output is selected as the performance indicator and used to derive the objective function of each cycle while the cycles' entropy generated is set as the minimization function. The work output to the heat input for the dual recuperative system was observed to be approximately 43%. Internal irreversibilities were observed to be significantly higher than the associated external irreversibility and in all cases considered, the receiver system was the dominant source of exergy loss. It is observed that the entropy generation due to the receiver, intercooler, and turbomachines increased with an increase in system mass flow rate. Irreversibility due to the recuperative system was fairly stable across all mass flow ranges. Geometric parameters of the HT recuperator were found to be of a higher value compared to its LT counterpart for all the system's mass flow rates. This aligns with our expectations as a larger surface area of the former is required for improved waste heat recovery. The single and dual regenerative system net power output peaks at approximately the same mass flow rate, with the latter producing 33.5% more work than the former. The dual recuperative system was observed to generate more net work at higher mass flow rates. On the contrary, with the increase was a substantial increase in its internal irreversibilities.

An improvement in the exergy use was observed in the first model, as its first and second law efficiency peaks at 44.9% and 59.68% respectively. A net work output to total heat input of 43% was obtained in Cases 1 and 2 while 42% was recorded in Case 3. It was observed more net power was recorded for Case 1, however, the ratio of net work output to the total heat input remains the same as in Case 2. The reheater is useful for an improved TIT and subsequently enhanced net work output from the system but its attendant irreversibility is a cause for concern.

Thus, the impact of the combined regenerative system should be compared with experiments and subjected to further analysis in the near future. These areas could be in the use of ductless receivers which would reduce complexities arising from installation, operation, and maintenance; optimization of duct lengths; and thermo-economic study performed on the system. Also, the impact of the turbomachines efficiencies on STBC systems can be examined to size the system adequately. This would ensure a total assessment of the technical prowess of the STBC as a means of generating electricity.

Declaration of Competing Interest

The authors declare that they have no known competing financial interests or personal relationships that could have appeared to influence the work reported in this paper.

References

[1] Jansen E, Bello-Ochende T, Meyer J. Integrated solar thermal Brayton cycles with either one or two regenerative heat exchangers for maximum power output. Energy 2015;86:737–48. doi: https://doi.org/10.1016/j.energy.2015.04.080.

[2] Tang C, Chen L, Feng H, Wang W, Ge Y. Tang, Power optimization of a modified closed binary brayton cycle with two isothermal heating processes and coupled to variable-temperature reservoirs. Energies 2020;13(12):3212.

[3] Chen L, Zhang Z, Sun F. Thermodynamic modeling for open combined regenerative brayton and inverse brayton cycles with regeneration before the inverse cycle. Entropy 2012;14:58–73. doi: https://doi.org/10.3390/e14010058.

[4] Forsberg CW, Peterson PF, Zhao H. High-temperature liquid-fluoride-salt closed-brayton-cycle solar power towers. J Sol Energy Eng Trans ASME 2007;129(2):141–6.

[5] Tyagi SK, Chen J, Lin G, Kaushik SC. Effect of several irreversibilities on the thermo-economic performance of a realistic Brayton heat engine cycle 2005;43:612–9.

[6] Khaleel OJ, Basim Ismail F, Khalil Ibrahim T, bin Abu Hassan SH. Energy and exergy analysis of the steam power plants: A comprehensive review on the Classification, Development, Improvements, and configurations. Ain Shams Eng J 2022;13(3):101640.

[7] Bahiraei M, Mazaheri N, Hanooni M. Employing a novel crimped-spiral rib inside a triple-tube heat exchanger working with a nanofluid for solar thermal applications: Irreversibility characteristics. Sustain Energy Technol Assessments 2022;52:102080.

[8] Mazaheri N, Bahiraei M, Razi S. Second law performance of a novel four-layer microchannel heat exchanger operating with nanofluid through a two-phase simulation. Powder Technol 2022;396:673–88.

[9] Chen L, Feng H, et al. Power and efficiency optimization for open combined regenerative brayton and inverse brayton cycles with regeneration before the inverse cycle. Entropy 2020;22:677. doi: https://doi.org/10.3390/E22060677.

[10] Andreades C, Scarlat RO, Dempsey L, Peterson P. Reheat-air brayton combined cycle power conversion design and performance under nominal ambient conditions. J Eng Gas Turbines Power 2014;136:1–12. doi: https://doi.org/10.1115/1.4026506.

[11] Stijepovic MZ, Papadopoulos AI, Linke P, Stijepovic V, Grujic AS, Kijevčanin M, et al. Organic Rankine Cycle system performance targeting and design for multiple heat sources with simultaneous working fluid selection. J Clean Prod 2017;142:1950–70. doi: https://doi.org/10.1016/j.jclepro.2016.11.088.

[12] Tyagi K. Detailed Experimental Measurements of Heat Transfer Augmentation in Internal Channels Using a Thermochromic Liquid Crystal Technique Detailed Experimental Measurements of Heat Transfer Augmentation in Internal Channels Using a Thermochromic Liquid Crystal; 2015.

[13] Adibi T et al. Investigating Effect of Intercooler on Performance and Efficiency of Brayton Cycle in Ideal and Non-ideal Condition. J Sci Eng Technol Res 2017;6:706–10.

[14] Haseli Y. Efficiency of irreversible Brayton cycles at minimum entropy generation. Appl Math Model 2016;40:8366–76. doi: https://doi.org/10.1016/j.apm.2016.04.031.

[15] Meas MR, Bello-Ochende T. Thermodynamic design optimisation of an open air recuperative twin-shaft solar thermal Brayton cycle with combined or exclusive reheating and intercooling. Energy Convers Manag 2017;148:770–84. doi: https://doi.org/10.1016/j.enconman.2017.06.043.

[16] Le Roux W, Bello-Ochende T, Meyer JP. Operating conditions of an open and direct solar thermal Brayton cycle with optimised cavity receiver and recuperator. Energy 2011;36:6027–36. doi: https://doi.org/10.1016/j.energy.2011.08.012.

[17] Le Roux W, Bello-Ochende T, Meyer J. Optimum Small-Scale Open and Direct Solar Thermal Brayton Cycle for Pretoria, South Africa. In: Proc. ASME 2012 6th Int. Conf. Energy Sustain. 2013: 1225. https://doi.org/10.1115/es2012-91135.

[18] Bejan A, Tsatsaronis G, Michael M. Thermal Design and Optimization 1996.

[19] Jin HG, Hong H. Hybridization of concentrating solar power (CSP) with fossil fuel power plants. In: Conc. Sol. Power Technol., Elsevier; 2012, pp. 395–420. https://doi.org/10.1533/9780857096173.2.395.

[20] Ogunmodimu O, Okoroigwe EC. Concentrating solar power technologies for solar thermal grid electricity in Nigeria: A review. Renew Sustain Energy Rev 2018;90:104–19. doi: https://doi.org/10.1016/j.rser.2018.03.029.

[21] Loni R, Askari Asli-Ardeh E, Ghobadian B, Bellos E, Le Roux WG. Numerical comparison of a solar dish concentrator with different cavity receivers and working fluids. J Clean Prod 2018;198:1013–30. doi: https://doi.org/10.1016/j.jclepro.2018.07.075.

[22] Sendhil N, Reddy K. Comparison of receivers for solar dish collector system. Energy Convers Manag 2008;49:812–9. doi: https://doi.org/10.1016/j.enconman.2007.07.026.

[23] Pavlovic S, Daabo AM, Bellos E, Stefanovic V, Mahmoud S, Al-Dadah RK. Experimental and numerical investigation on the optical and thermal performance of solar parabolic dish and corrugated spiral cavity receiver. J Clean Prod 2017;150:75–92. doi: https://doi.org/10.1016/j.jclepro.2017.02.201.

[24] F. et al. Ayalew, Optimization Techniques in Power System: Review, Int. J. Eng. Appl. Sci. Technol. 3 (2019) 8–16. https://doi.org/10.33564/ijeast.2019.v03i10.003.

[25] Tang C, Chen L, Feng H, Ge Y. Tang, Four-objective optimizations for an improved irreversible closed modified simple brayton cycle. Entropy 2021;23(3):282.

[26] S.D. Dao, A Note On The Popularity of Stochastic Optimization Algorithms in Different Fields: A Quantitative Analysis from 2007 to 2017, ArXiv. (2019).

[27] Wang X, Damodaran M. Comparison of deterministic and stochastic optimization algorithms for generic wing design problems. J Aircr 2000;37:929–32. doi: https://doi.org/10.2514/2.2695.

[28] Haji Haji V, Monje CA. Fractional order fuzzy-PID control of a combined cycle power plant using Particle Swarm Optimization algorithm with an improved dynamic parameters selection. Appl Soft Comput J 2017;58:256–64. doi: https://doi.org/10.1016/j.asoc.2017.04.033.

[29] Garrett, Turbomachines data sheet, 2019; 1–2.

[30] Roux WG, Bello-Ochende T, Meyer JP. Thermodynamic Optimisation of the Integrated design of a small-scale solar thermal Brayton cycle. Int J Energy Res 2012;36(11):1088–104.

[31] Reddy KS, Kumar NS. An improved model for natural convection heat loss from modified cavity receiver of solar dish concentrator. Sol Energy 2009;83:1884–92. doi: https://doi.org/10.1016/j.solener.2009.07.001.

[32] Stine B, Harrigan R. Solar energy fundamentals and design. New York: John Wiley & Sons; 1985.

[33] Stine WB, Geyer M. Power Cycles for Electricity Generation. Power from Sun 2001:1–28. , http://www.powerfromthesun.net/Book/chapter12/chapter12.html.

[34] Abraham JP, Sparrow EM, Minkowycz WJ. Internal-flow Nusselt numbers for the low-Reynolds-number end of the laminar-to-turbulent transition regime. Int J Heat Mass Transf 2011;54:584–8. doi: https://doi.org/10.1016/j.ijheatmasstransfer.2010.09.012.

[35] Kumar R, Kaushik SC, Kumar R, Hans R. Multi-objective thermodynamic optimization of an irreversible regenerative Brayton cycle using evolutionary algorithm and decision making. Ain Shams Eng J 2016;7(2):741–53.

[36] Jubeh NM. Exergy analysis and second law efficiency of a regenerative Brayton cycle with isothermal heat addition. Entropy 2005;7:172–87. doi: https://doi.org/10.3390/e7030172.

[37] Kotas TJ, Mayhew YR, Raichura RC. Nomenclature for exergy analysis (Kotas 1995).pdf. J Power Energy 1995;209(4):275–80.

[38] Nabab M. Particle Swarm Optimization: Algorithm and its Codes in MATLAB. ResearchGate 2016:8–12. doi: https://doi.org/10.13140/rg.2.1.4985.3206.

O.M. OYEWOLA: He is a full professor of thermofluids and energy at Fiji National University, Fiji.

M.O. PETINRIN: He is a Senior Lecturer with areas of interest in thermofluids and energy at University of Ibadan, Nigeria.

M.J. LABIRAN: He is a researcher in thermofluids and energy at University of Ibadan, Nigeria

T. BELLO-OCHENDE: He is a full professor of thermofluids and energy at University of Cape Town, South Africa.